Processing and Characterization of HfB_2 and ZrB_2 Based Solid Solution Composites for Magnetohydrodynamic (MHD) Power Generation Applications

A Thesis
Presented in Partial Fulfillment of the Requirements for the
Degree of Master of Science
with a
Major in Materials Science and Engineering
in the
College of Graduate Studies
University of Idaho
by

Cody D. Hill

Major Professor: Indrajit Charit, Ph.D.
Committee Members: Krishnan S. Raja, Ph.D; Mark F. Roll, Ph.D
Department Administrator: D. Eric Aston, Ph.D.

December 2015

Authorization to Submit Thesis

This Thesis of Cody D. Hill, submitted for the degree of Master of Science with a Major in Materials Science and Engineering and titled "Processing and Characterization of HfB_2 and ZrB_2 Based Solid Solution Composites for Magnetohydrodynamic (MHD) Power Generation Applications," has been reviewed in final form. Permission, as indicated by the signatures and dates below, is now granted to submit final copies to the College of Graduate Studies for approval.

Major Professor: _____ Date: _____
Indrajit Charit, Ph.D.

Committee Members: _____ Date: _____
Krishnan S. Raja, Ph.D.

_____ Date: _____
Mark F. Roll, Ph.D.

Department Administrator: _____ Date: _____
D. Eric Aston, Ph.D.

Abstract

Magnetohydrodynamic direct power extraction can potentially increase the efficiency of power generation in coal-based power plants by producing electricity directly out of ionized exhaust, through the use of electrodes. Transition metal diborides, such as HfB_2 and ZrB_2, show promise as a material for such electrodes. Despite research on individual borides, little is known about the mechanical, electrical, thermal, and oxidation resistance of HfB_2-ZrB_2 solid solutions for the MHD electrode application. In the present work, spark plasma sintering was used to consolidate HfB_2-ZrB_2 powder prepared by high energy ball milling. Microstructural characteristics of both the milled powders and SPSed specimens were studied by X-ray diffraction and scanning electron microscopy. Density, Vickers micro-indentation hardness, indentation fracture toughness and electrical resistivity of such SPSed specimens were measured. Also examined were the effects of additives, Gd_2O_3, LaB_6, Hf, Zr, and Ta, on $Hf_{0.5}Zr_{0.5}B_2$, which generated greater densification and smaller grain size.

Acknowledgements

I would like to thank my advisor Dr. Indrajit Charit and co-advisor Dr. Krishnan S. Raja for their support and guidance. Their abetment in my writing and their reviewing of my submitted work has been momentous. I would also like to take the chance to thank them for allowing me to travel abroad for a conference and present my research. I would like to thank Dr. Mark F. Roll for residing on my committee and his discussions and guidance for my thesis.

Additionally, I would like to acknowledge the DOE-NETL University Coal Research Program under the direction of Dr. Jason Hissam for funding the research under grant DE-FE0022988. I would like to acknowledge Mr. Bryan L. Forsmann for his intellectual guidance and help with operating the SPS instrument at the Center for Advanced Energy Studies, as well as, for taking photographs of SPS operations shown during Section 3.2. I would like to thank Dr. Thomas J. Williams at the Center for Electron Microscopy & Microanalysis for allowing me extended usage of his facility.

Dedication

I would like to dedicate this thesis to my loving wife, Sunbeam, whose inspiration, sacrifice, and inexhaustible patience made possible its completion, and to Sequoia Genevieve, to whom I am eternally indebted.

Table of Contents

List of Figures

List of Tables

1. Introduction

1.1 Introduction

Development of electrode materials capable of operating continuously in a corrosive environment and temperatures in excess of 2500 °C is critical for advancement of Magnetohydrodynamic (MHD) direct power extraction. Next generation clean coal power plants rely on power extraction methods that are more efficient than conventional coal-fire steam plants. In addition to being able to withstand high temperature exposure, the material should exhibit hot corrosion resistance, oxidation resistance, high electrical and thermal conductivity, and be cost effective.

Zirconium diboride (ZrB_2) and hafnium diboride (HfB_2) are transition metal diborides (TMB), which belong to a class of ultra-high temperature ceramics (UHTC). Similar to many transition metal diborides, ZrB_2 and HfB_2 are characterized by having a P6/mmm space group. The bonding of ZrB_2 and HfB_2 is comprised of TM-B bonds with ionic and covalent character, B-B covalent bonds, and TM-TM metallic bonds. The presence of the bonding combinations in TMB is responsible for many unique properties. ZrB_2 and HfB_2 exhibit chemical inertness even at high temperatures, high thermal conductivity, high electrical conductivity, high strength, adequate shock resistance, and very high melting points, in excess of 3000 ^oC. This type of materials has the potential to be used as MHD electrodes and further in-depth investigation is needed. The electrical resistivity of sintered ZrB_2 - HfB_2 solid solutions have not been investigated and data are not available in open literature. Thus, one of the purposes of the thesis research was to systematically investigate the effect of ZrB_2-HfB_2 solid solutions on the electrical resistivity, as well as, the effect of additives on the electrical resistivity of the

lowest resistivity ZrB_2-HfB_2 solid solution. The research presented herein addresses some fundamental questions including:

1. What effect do additives have on the crystal structure and microstructure of ZrB_2 - HfB_2 solid solutions?
2. What additives have the greatest effect on densification and sinterability of ZrB_2-HfB_2 solid solutions, without affecting the crystal structure?
3. Which ZrB_2-HfB_2 solid solution has the lowest electrical resistivity?

Taken in its entirety, the research delineated in this thesis has the potential to improve our understanding of the ability of ZrB_2 and HfB_2 to form extensive solid solutions without and with the additions of different dopants, and the effect of the mole ratio of ZrB_2 in ZrB_2-HfB_2 solid solutions on electrical resistivity. Furthermore, the research described herein may provide a basis for minimizing electrical resistivity in ZrB_2 - HfB_2 solid solutions.

2. Literature Review

2.1 Magnetohydrodynamic Direct Power Generation.

Magnetohydrodynamics can be regarded as the dynamics of electrically conductive fluids in the presence of electric and magnetic fields. In an ionized gas, there exists a large number of corpusculum with a net positive charge and others with a net negative charge. The presence of an external electrical field will influence the charged corpuscles with forces in directions based on the net charge of the corpusculum.

In a simple MHD direct power extraction system, coal-fire exhaust is guided into a tight jet, forming a plasma. The plasma may be aspirated with a potassium salt to increase the conductivity; although He/Xe has also been considered as a working fluid and plasma seed, respectively [1]. From an economic standpoint, coal fired MHD power generation will be the most favored. The plasma is channeled through a permanent transverse magnetic field, as shown in Figure 2.1.

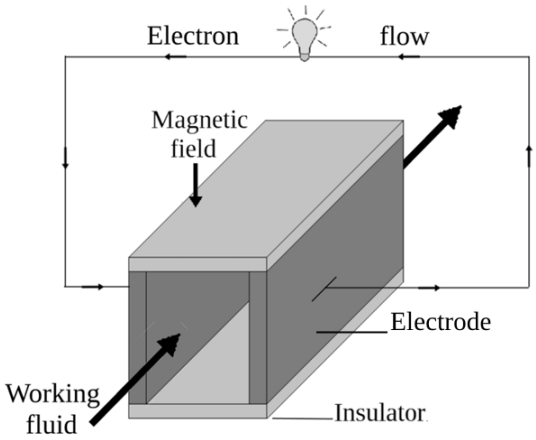

Figure 2.1 A schematic representation of the MHD direct power extraction circuit: The orientation of the MHD electrode is orthogonal to that of the magnetic field and the flow of the working fluid.

The energetic ions in the plasma motion are deflected according to the Lorentz force law, Equation 2.1. The deflected ions collide with the electrode surfaces, building up a surface charge. When the electrode surfaces are connected electrically, a DC potential is extracted.

$$\vec{F} = eZ\vec{E} + eZ\vec{\omega} \times \vec{B} \tag{2.1}$$

where $\vec{F}$ is the Force acting on the ion of charge (q), traveling at velocity (v), through a permanent magnetic field ($\vec{B}$). For a simple MHD power plant utilizing a permanent magnet, the electric field ($\vec{E}$) can be taken to be zero [2].

2.1.1 Motion of charged particles in a uniform magnetic field

Consider a particle with a net number of charge *(Z)* with velocities parallel and perpendicular to the magnetic field, $\omega_{\parallel}$ and $\omega_{\perp}$ respectively. From the Lorentz force, the force felt on the charge particle is eZ**ω** X **B**. The plane of motion of the charged particle will be circular. The acceleration on the charged particle will be the ratio of the particles velocity perpendicular to the magnetic field and the radius of curvature of the path, $\omega_{\perp}/r_{L.}$ Application of Newton's law can yield the cyclotron frequency, w, shown in Equation 2.2 [3].

$$w = \frac{\omega_{\perp}}{r_L} = \frac{eZ\boldsymbol{B}}{m} \tag{2.2}$$

The cyclotron motion of the charged particle in the presence of an eternal magnetic field is shown in Figure 2.2. It is noted that a particle with charge (-*Z*) will undergo cyclotron motion in a counter-clockwise direction [2].

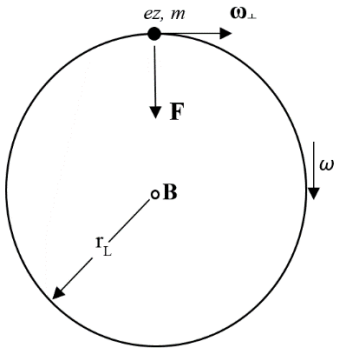

Figure 2.2 The cyclotron motion of a charged particle in a constant magnetic field.

2.1.2 Historical attempts at MHD direct power generation

It was not until 1940 that the first MHD power plant design was patented [4]. The first MHD power generator, (UO2), was built in the 1960s near Moscow, by the erstwhile U.S.S.R. During initial operation, 0.2 kW was achieved. After two years of experimenting, the facility was able to make 42 kW of power [5].

After the initial trial at the (UO2) facility, a larger (U25) facility was built in the USSR in 1975. The facility featured a 250 MW input capacity, utilizing natural gas burners and a superheated oxygen enriched air. During initial trials, the facility yield 7 MW of power [5]. After much experimenting, (U25) was generating 25 MW of power. The power was solely extracted utilizing the MHD direct power extraction, no further power extraction of the MHD exhaust was employed [5].

U-25B MHD generator was built as a cooperative program between the USSR and the U.S. The U-25B was built as a test facility bypass loop at the U-25 MHD power plant near Moscow. The Argonne National Laboratory provided a 5-T superconducting magnet system to test at the U-25B. The magnitude of the 5-T magnet allowed for experiments during high

electromagnetic interactions and high flow, which simulated proposed commercial MHD power plant operating conditions [6].

From the information gained at the U-25B, the component development and integration facility (CDIF) was built in Butte, Montana in 1981. CDIF was based on coal as a fuel rather than natural gas. The pilot facility at CDIF was based on 50 MW of thermal input. The first coal-fired testing of the CDIF pilot facility was conducted in 1985, yielding 1.51 MW power [5].

In 1981 the Shanghai power plant research institute conducted a MHD-Steam combination power generator, in which the MHD exhaust was used to generate steam and drive a steam turbine [7]. The facility was operated for 150 continuous hours. During the tests, 514.9 kW was generated, with 500 kW from the steam portion [5].

Most past attempts at MHD direct power generation employed oxide based electrodes [7]. Oxide materials are intrinsically resistant to oxidation. However, the characteristics of conventional oxide materials limit their functionality, due to their high electrical resistivity, low thermal conductivity, and high volatility at MHD operating conditions. Since the melting point of most of the oxides is less than 2000 ^{0}C early examples of MHD direct power generation power plants failed to operate for extended periods of time without heavily cooling the electrodes [7].

Strontium doped $LaCrO_3$, was considered the best oxide material candidate electrode materials for MHD power generation [8] despite its poor electrical characteristics during MHD power plant conditions.

The development of MHD direct power plants will utilize next generation electrode materials that show high electrical and thermal conductivity infused with better stability in the aggressive high temperature environments.

2.2 Ultra-High Temperature Ceramics

Ultra-high temperature ceramics (UHTC) are classified as ceramic materials with melting points above 3000 ^{o}C [9]. Common examples of UHTCs are thoria, transition metal diborides, transition metal carbides, and tantalum nitride and hafnium nitride [10]. According to Barsoum [11] ceramics are, "Solid compounds that are formed by the application of heat, and sometimes heat and pressure, comprising at least one metal and a non-metallic elemental solid, a combination of at least two nonmetallic elemental solids, or a combination of at least two nonmetallic elemental solids and a nonmetal."

2.2.1 Transition Metal Borides

As a transition metal boride, ZrB_2 and HfB_2 is classified as a UHTC material. These ceramics are noted by their melting point of over 3000 °C. This particular family of compounds is characterized with having enhanced refractoriness and chemical stability at high temperatures [10].

Transition metal borides (TMB) are desirable for the development of electrode materials for high temperature applications. The properties of TMB, due to their bonding and crystallography, are characterized by high melting point, high electrical and thermal conductivities, high strength and hardness up to elevated temperatures, and chemical inertness [10].

2.2.1.1 Crystallography and Bonding

Electronic structure and bonding properties of TMB have been calculated from first principles in many studies [12-14]. Chemical structure, ground-state properties, and bonding have been calculated by Vajeeston *et al*, using self-consistent tight-binding linear muffin-tin orbital method [12]. The elastic properties, and specific heat of HfB_2 and ZrB_2 were calculated by Lawson *et al.*, using DFT codes [13].

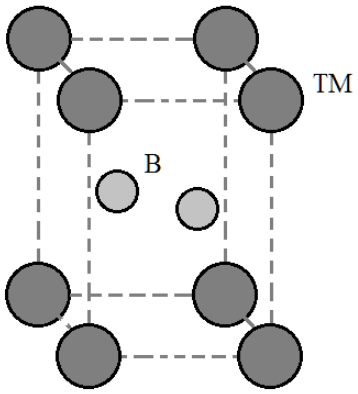

Figure 2.3. Unit cell of AlB_2 type P6/mmm hexagonal crystal structure.

The positions of the atoms in the P6/mmm hexagonal structure of TMB are given as Wyckoff positions as follows: TM (0,0,0), B(1/2,2/3,1/2), the unit cell of which is shown in Figure 2.3 [10]. Published experimental and calculated lattice parameters are given in Table 2.1.

Table 2.1 Lattice constants of ZrB_2 and HfB_2.

Lattice Constants (Å)	ZrB_2	HfB_2	
a_{exp}	3.170	-	[10]
a_{calc}	3.197	3.166	[12]
	3.170	3.150	[13]
c_{exp}	3.53	-	[10]
c_{calc}	3.561	3.499	[12]
	3.560	3.520	[13]

2.2.1.2 Electrical and Thermal Properties

Studies have reported the thermal and electrical resistivity for ZrB_2 and HfB_2 with and without various additives [15-20]. Selected published electrical resistivity and thermal conductivity data as a function of temperature are shown in Figure 2.4.

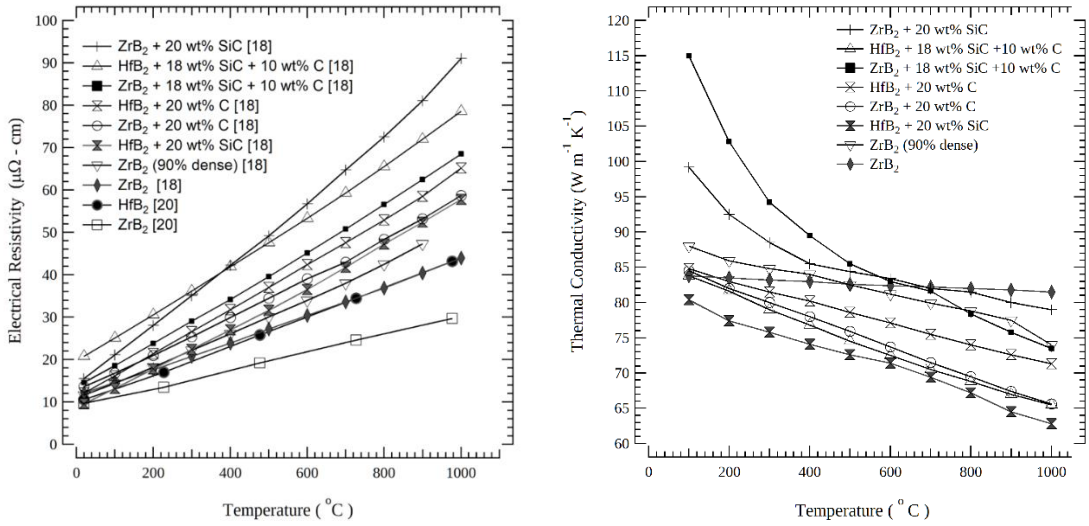

Figure 2.4. Electrical resistivity (*left*) and thermal conductivity (*right*) of zirconium and hafnium diboride based ceramics as a function of temperature. Thermal conductivity data was adapted from data obtained by Tye and Clougherty *et al* [18].

2.2.1.3 Mechanical Properties

According to literature, the range of elastic modulus at room temperature for ZrB_2 is from around 350 to 530 GPa [21- 26] and flexure strengths with and without sintering aids were found to be between 250 and 630 MPa [27-32]. The majority of reported values for fracture toughness of ZrB_2 is roughly 3.5 MPa·$m^{½}$, with an average range of 3.0-4.5 MPa·$m^{½}$ [33-39]. The variations depend on additives, grain size, and porosity. Room Temperature hardness values for ZrB_2-SiC composites range between 17-27 MPa depending on sintering method, final densification, and mass percent of SiC added [40-44]. Room temperature

Vickers hardness ranges between 21-23 GPa for monolithic ZrB_2 and was 28 GPa for monolithic HfB_2 [33, 45].

2.2.1.4 Oxidation Resistance

During MHD direct power generation conditions, the electrodes are subjected to oxidative conditions. The hafnium diboride and zirconium diboride based electrode materials will oxidize based on the following equations [46]:

$$ZrB_{2(s)} + \frac{5}{2}O_{2(g)} \rightarrow ZrO_{2(s)} + B_2O_{3(l)} \quad (2.3)$$

$$HfB_{2(s)} + \frac{5}{2}O_{2(g)} \rightarrow HfO_{2(s)} + B_2O_{3(l)} \quad (2.4)$$

$$B_2O_{3(l)} \rightarrow B_2O_{3(g)} \quad (2.5)$$

The effect of aspirated potassium salt in the MHD exhaust on the boride based electrode materials is not known and is not presented in the following work.

2.2.2 Effect of Additives

Because of the strongly covalent nature of ZrB_2 and HfB_2 and high melting point, sintering to full density is difficult. The addition of sintering aids can greatly increase final density of conventional sintering methods; however it can adversely affect the final properties of the materials. For example, the formation of ZrB_2-SiC has been shown to increase final densification; however, ZrB_2-SiC forms a eutectic, reducing the liquidous temperature down to 2300 ^oC [47].

2.2.2.1 Addition of SiC

The addition of SiC to transition metal diborides has been widely studied. ZrB_2-SiC composites have been shown to have excellent mechanical properties at room temperature. The addition of SiC to ZrB_2 has been shown to increase room temperature fracture toughness up to 5.5 MPa $m^{1/2}$ [33, 43, 48]. Hardness values measured at room temperature can be as high as 22 GPa [33, 49, 50], and strengths have been shown to be over 1000MPa [33, 48, 49]. At temperatures above 1600 ^oC, SiC has been shown to have detrimental effects.

The effect of SiC on the reduction of solidus temperature and the high vapor pressure of ZrB_2-SiC above 1865 ^oC limits the viability of exploration into this material for extreme temperature electrodes. It has been found that the oxidation resistance of ZrB_2 can be improved at temperatures below 1600 ^oC by the addition of 20-30 vol% of SiC. SiC preferentially oxidizes over ZrB_2 and forms a glassy layer with B_2O_3 [51]. As the temperature exposed to the surface exceeds 1600 ^oC, SiC oxidization rates increase forming several liquid and gaseous phases, such as SiO_2, and SiO, shown in Equation 2.6.

$$SiC_{(s)} + \frac{3}{2}O_{2_{(g)}} \rightarrow SiO_{2_{(l)}} + CO_{(g)} \qquad (2.6)$$

According to calculations by Opeka *et al*, the vapor pressures are the highest at the Si-SiO_2 interface and the SiO interfacial vapor pressure exceeds 10^5 Pa at 1865 °C. The pressure gradient on the free surface will rupture the borosilicate protective layer and result in break-away oxidation of SiC at temperatures greater than 1865 °C [51]. Furthermore, SiO when exposed to water vapor at elevated temperatures forms $Si(OH)_4$, which leads to further loss of material [52-54].

2.2.2.2 Addition of Gd_2O_3

It has been shown that addition of Gd_2O_3 to transition metal diborides can effectively increase the oxidation resistance of the material. In a study by Zapata-Solvas *et al*, it was shown that with the addition of 10 wt% Gd_2O_3, oxidation rates at 1600 ^oC were hindered due to the formation of heterogeneous crystalline oxides in an intermediate layer between the bulk and the oxide scale. The addition of Gd_2O_3 maintained the integrity of the oxide scale up to 1600 ^oC [52]. The effect of Gd_2O_3 on TMB solid solutions without that presence of SiC is currently unknown and will be explored in the present work.

2.2.2.3 Addition of LaB_6

In a study by Zhang *et al*, the oxidation resistance of ZrB_2–SiC–LaB_6 composites were tested at temperatures greater than 2400 ^oC for 600 s using an oxyacetylene torch. The results of the study showed a subsequent growth of the oxide scale to a final thickness of 545 μm, and the sample underwent a subsequent loss of 0.2 wt% during the 600 s test [55].

If the results of Zhang *et al's*, study were extrapolated over a longer time frame to simulate MHD direct power extraction conditions, the oxide scale will increase 7.85 cm/day in thickness and the material will undergo a loss of 28.8 wt% per day. The ZrB_2–SiC–LaB_6 composite alloy will function for leading edges of hypersonic re-entry; however, in situations where oxidative conditions and high temperature exposure are longer than brief, the material will fail.

The presence of LaB_6 in TMB systems leads to the formation of dense TMO_2 scales when exposed to oxidation conditions in a static environment. The oxidation of lanthanum

hexaboride and formation of heterogeneous crystalline oxide film are given in the following equations [56]:

$$LaB_{6(s)} + \frac{21}{4}O_{2(g)} \rightarrow \frac{1}{2}La_2O_{3(s)} + 3B_2O_{3(l)} \qquad (2.7)$$

$$La_2O_{3(s)} + TMO_{2(s)} \rightarrow La_2TM_2O_{7(s)} \qquad (2.8)$$

The regenerative formation of the TMO_2 oxide scale is likely due to formation of liquid phases, which aid in the densification of the TMO_2 scale during brief oxidation [56].

2.2.2.4 Addition of Tantalum

The addition of tantalum (Ta) has been shown to increase oxidation resistance of TMB up to 1700 ^oC due to the substitution of Ta in the TM sites of TMO_2. The Kroger-Vink notation of the oxidization reaction of TMB bearing Ta additions is given in the following Equation [57]:

$$Ta_2O_5 + V\ddot{O} \xrightarrow{2ZrO_2} 2\,Ta_{\dot{Zr}} + 5O_0 \qquad (2.9)$$

A study by Talmy *et al*. [58] showed that oxidation resistance of ZrB_2-SiC composites could be enhanced by the addition of TaB_2; however, the improved oxidation resistance was shown to last only up to 1500 ^oC. It was suggested by Talmy *et al* [58], that the oxidation resistance of ZrB_2-20% v/o SiC with TaB_2 additions was due to Ta_2O_5 causing liquid immiscibility and subsequent phase separation in the borosilicate glass oxide layer.

In addition to studies utilizing TaB_2 as an aid to improve oxidation resistance, TaC and $TaSi_2$ have been explored. A study by Opila *et al*, showed that ZrB_2 - 20 vol% SiC + 20 vol% $TaSi_2$ resulted in low oxidation rates in stagnant air, when heated to 1627 ^oC. At higher temperatures; however, the formation of liquid phases drastically decrease the oxidation resistance at higher temperatures, likely due to the formation of a eutectic [59].

2.2.2.5 Effect of Boron/Metal Ratio

In a study by Manlabs Inc., the effects of boron/metal ratios on the electrical and chemical properties of hafnium diboride and zirconium diboride were addressed. The effect of boron/metal ratios on oxidative properties and sinterability was also studied. Metal rich hafnium boride and zirconium boride were found to reach higher final densities during similar sintering studies. $HfB_{1.89}$ exhibited the highest oxidation resistance throughout the range of study. Electrical resistivity was seen to decrease when boron/metal ratios were less than two. At boron/metal ratios above two, electrical resistivity increased, sinterability decreased, and oxidation resistance decreased [60].

2.3 Synthesis Techniques

Because transition metal borides do not readily occur in nature, the materials must be produced synthetically. The earliest reported synthesis of transition metal borides is from 1901 by Tucker and Moody [61], who reacted elemental zirconium and boron to form, what they thought was, Zr_3B_4. Carbothermal synthesis of ZrB_2 was later described by McKenna in 1936, in which ZrO_2, carbon, and B_2O_3 were reacted at 2000 ^oC to form ZrB_2 [62]. Due to the difficulties in separating hafnium and zirconium, the formation of HfB_2 was not described in literature until 1931 by Agte and Moers [63].

2.3.1 Sol-gel Route

Sol-gel is a synthesis technique to produce ceramics through the use of organic ligands and other chemical precursors. A sol is defined as “a stable suspension of colloidal solid particles within a liquid;” and a gel is defined as “a porous 3-dimensionally interconnected

solid network that expands in a stable fashion throughout a liquid medium and it is only limited by the size of the container" [64]. A sol-gel process is a synthesis technique originally considered to be restricted to gels synthesized from alkoxides. At present, many materials are synthesized by the sol-gel technique. A working definition for sol-gel process could be as follows: "a colloidal route to synthesize ceramics with an intermediate stage including a sol and/or a gel" [64]. In a study by Zhang *et al*, sol-gel synthesis was used to synthesize ZrB_2–SiC from zirconium *n*-propoxide, boric acid, sucrose, Tetraethyl orthosilicate, and acetic acid. It was found that the acetic acid could hydrolyze the zirconium *n*-propoxide without the use of the water in the aqueous solutions, although this was not confirmed by performing sol-gel synthesis with acetic acid as the solvent [65]. The sol-gel process can also be used to modify the surface chemistry of diboride powders. In a study by Ang *et al*, the surface of zirconium diboride was coated with a ZrO_2 and carbon based sol-gel. Nano sized crystalline ZrC grains formed on the surface of the ZrB_2 powder after a carbothermal reduction [66].

2.3.2 Reduction Synthesis

Reduction synthesis routes allow the use of less inexpensive reactants. The downside to reduction synthesis methods are residual impurities, and because the reduction of transition metal oxides is an endothermic reaction, high temperatures must be employed to make the reaction proceed favorably.

Carbothermal reduction of transition metal oxides in the presence of boric acid and carbon at temperatures above 1200 ^{o}C, will produce transition metal diborides following Equation 2.10 [67].

$$MeO_{2(s)} + B_2O_{3(l)} + 5C_{(s)} \rightarrow MeB_{2(s)} + 5CO_{(g)} \qquad (2.10)$$

Because boric acid has a high vapor pressure at the temperature of reduction, boric acid should be replenished during the reaction. A study by Zhao et al, showed that the addition of excess boric acid at the start of the reaction is required to compensate for the volatility of boric acid; Furthermore, the volatility of the boric acid was determined to be substantial at 1200 ^{o}C, while reduction temperatures were closer to 1400 ^{o}C [67].

For the boro/carbothermal reduction synthesis, boric acid and carbon are used to reduce transition metal oxides and form diborides. The boro/carbothermal reduction follows Equation 2.11 [68].

$$MeC + B_2O_3 + 2C \rightarrow 2MeB_2 + 3CO_{(g)} \qquad (2.11)$$

In a study by Qiu *et al.*, boro/carbothermal reduction synthesis was used to produce ZrB_2 particles of different sizes and geometries by varying the source of carbon and performing the reduction synthesis in different atmospheres. It was shown that using carbon black as the carbon source versus graphite reduced the reduction temperature under vacuum. The source of carbon did not have an effect on the temperature of the reduction when performed in argon. The shape of the resultant ZrB_2 was seen to be rodular shaped when performed under vacuum, and semi-spherical when performed in argon [68].

The boron carbide reduction of transition metal diborides follows Equation 2.12 [69].

$$2MeO_2 + B_4C \rightarrow 2MeB_2 + 4CO_{(g)} \qquad (2.12)$$

In a study by Jung *et al*, boron carbide reduction was determined to be the most favorable boron/carbon reduction synthesis approach to form ZrB_2, due to limited rodular growth of ZrB_2 and little B_2O_3 impurities. The residual B_2O_3 impurities were found to be easily removed by successive methanol washes [69].

Borothermal reduction is the reduction of transition metal diborides with boron. Borothermal reduction follows Equation 2.13 [70],

$$MeO_2 + 4B \rightarrow MeB_2 + B_2O_{2_{(g)}} \qquad (2.13)$$

In a study by Peshev *et al*, titanium, hafnium, and zirconium diboride were formed under vacuum by borothermal reduction synthesis. It was discovered that, ZrB_2 formed at higher temperatures and after longer reaction times than HfB_2 and TiB_2. TiB_2 was obtained when the reduction reaction was performed at 1700 ^oC for 1 h, and HfB_2 was obtained after 2 h at 1750 ^oC [70].

The magnesiothermic reduction of transition metal oxide and boric acid by magnesium occurs through a liquid-liquid-solid phase process, following Equation 2.14. The reaction is a self-propagating reaction [71].

$$Mg + B_2O_3 + MeO_2 \rightarrow MgO + MeB_2 \qquad (2.14)$$

The magnesiothermic reduction synthesis of ZrB_2 is thought [71] to be a three phase process. First, at 650 ^oC liquid Mg and B_2O_3 is formed, and solid ZrO_2 and glassy B_2O_3 collects on the surface of the liquid magnesium. Second, dissolution-precipitation reactions form Zr and MgO, releasing copious amounts of heat. The copious amount of heat drives the diffusion reaction between Mg and boric acid, forming B and MgO, and finally Zr and B react to form ZrB_2, releasing further energy to drive the reaction.

In a study by Setoudeh, a magnesiothermic reduction synthesis of ZrB_2 was performed in a differential thermal analysis apparatus. It was concluded that multiple reactions occurred simultaneously, all leading to the formation of ZrB_2. It was also concluded that successive washes in mild acid would remove the MgO contaminates [72].

2.3.3 Elemental synthesis

Reactions of elemental transition metals with elemental boron is a highly exothermic reaction. Self-propagating reactions for the synthesis of transition metal diborides can be ignited at room temperature, following Equations 2.15, 2.16 [74].

$$Zr + 2B \rightarrow ZrB_2 \qquad \Delta G_{rxn,\ 298K} = -318\ \text{kJ/mol} \qquad (2.15)$$

$$Hf + 2B \rightarrow HfB_2 \qquad \Delta G_{rxn,\ 298K} = -325\ \text{kJ/mol} \qquad (2.16)$$

Elemental synthesis is a favorable route due to the high rates of heating and cooling, which lead to increased defect rates. The presence of defects allows a higher rate of densification when sintering the transition metal diborides into bulk [73]. The main drawback of elemental synthesis is the cost of the precursors and the pyrophoricity of transition metal powders. A study by Aviles *et al*, showed that hafnium diboride zirconium diboride solid solutions can be synthesized by self-propagating synthesis via ball milling [74].

2.4 Powder Processing

Powder processing may refine the transition metal borides to induce microstructural strain and defects which may aid in sintering rates and densification. High energy milling is commonly employed to reduce particle diameters. The reduction of particle diameters may aid in compaction.

2.4.1 High-energy Milling

A method of mechanically alloying is performed through high-energy milling and is defined as the continual pattern of cold welding, fracturing, and re-welding [75]. The mechanical breakdown of solids without changing the state of aggregation is defined as

milling. Milling increases the surface energy of solids by introducing defects and strain in the aggregate [76]. The increase in surface energy arises as the surface area is drastically increased with the reduction of size. The effect of increased surface energy in milled aggregates can be used to produce materials for catalysis, adsorption media, or initial materials for sintering [77]. Milling can be used to create particles of certain shapes and mean sizes, depending on the crystal structure of the solid to be milled, the size and loading of the milling media. Much of the energy consumed during high energy milling can be attributed to generation of heat, and plastic deformation of the media, vial, and material to be milled [78, 79]. The main contributions of forces leading to size reduction are compression, shear, and impact; however, the reduction in powder size is often complicated by cold welding of the particles into larger agglomerates [75]. Studies show that there is a minimum size that the powder can become given certain milling conditions, whereupon increased milling time will cause the powder particles to cluster into larger entities. [80].

The main types of high energy mills used during ceramic studies are ball, attrition, and mixer mills. The primary types of mechanical stress interactions during milling are compression, shear, and impact.

2.4.1.1 Ball Mills

Ball mills feature a vial that is set in angular motion around the longitudinal axis of the vial. Around 50% of the total volume within the vial is filled with grinding media and material. The angular velocity of the vial is an important attribute for the efficiency of a ball mill. The speed of rotation of a vial determines the mode of motion of the grinding media

[81]. The three major modes of motion are cascading, falling, and centrifugal. The modes of motion are depicted in Figure 2.5.

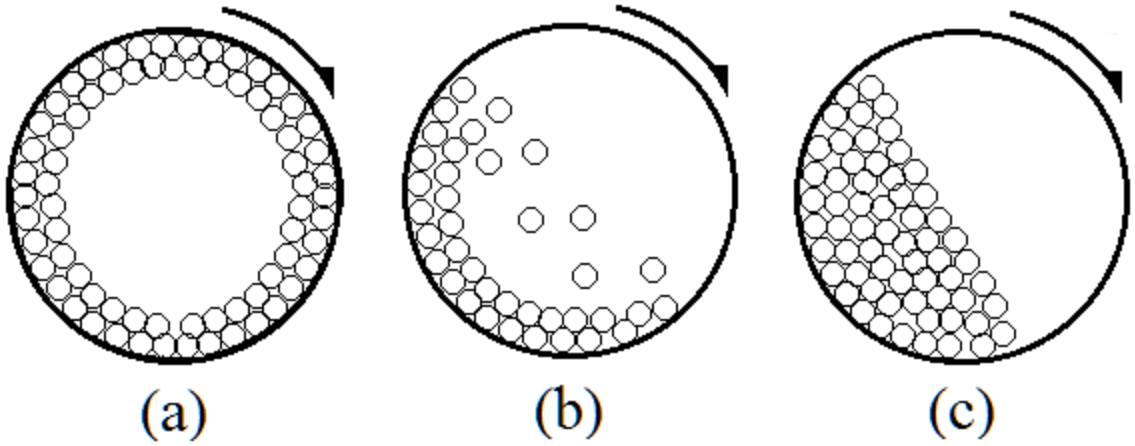

Figure 2.5 Types of motion in a ball mill vial: centrifugal (a), falling (b), and cascading (c).

Cascading motion is ideal because it provides controlled interaction between the grinding media and the material. Cascading motion will minimize hard impacts, falling motion may lead to excessive impurity levels, and centrifugal motion minimizes collisions of grinding media therefore lengthening the mill time [82]. Adding equally spaced lifters to the inner volume of the vile act to minimize centrifugal motion of the grinding media. If there are no lifters in the mill, the balls will take preferential paths [83].

2.4.1.2 Attrition Mill

The basic operating configuration of an attrition mill is a stationary vial, with 80% of its internal volume filled with grinding media, material, and mixing fins attached to a stirring [84]. The stirring rod is oriented along the longitudinal axis of the internal volume of the vile. Milling action is achieved by rotation of the stirring fins, causing the milling media to grind the material [85]. Benefits of attrition mill are the reduction of amorphization of the material

as compared to other types of mills [86]. Milling media is usually in the shape of spheres and should be between 0.5 to 4 mm [87].

2.4.1.3 Mixer Mills

The mixer mill is considered a very high-energy mill [88]. In mixer mills the vial performs a motion in space, described as a back and forth motion, coupled with lateral movements at each ends of the vial. These motions can be carried out several thousand times per minute. Certain mixer mills can provide peak amplitudes of movement up to 50 mm at a frequency of 20 Hz. The advantage of the motion is that it causes grinding media to take a more dynamic path, leading to enhanced chaotic collisions [82]. The increased collisions reduce mill time. After roughly 4 h of milling in a SPEX mixer mill, particle sizes have been shown to be less than 20 nm [89-91].

2.4.2 Milling conditions

In addition to the type of mill used, milling conditions can be optimized to increase the efficacy of the milling operation. Milling conditions, such as ball-to-powder ratio can affect the levels of impact energy between the powder, balls, and the vial walls [92]. The type of grinding media utilized determines the efficacy of the milling. Grinding media that is not matched to the vial material or the powder composition will lead to impurities or incomplete milling [92]. Milling can be performed under many atmospheres and with or without the presence of process control agents [93].

2.4.2.1 Grinding Media

The preferred grinding media are made from materials with good to excellent wear resistance, while exhibiting a density close to or higher than the material to be milled. Some examples of frequently used grinding media are tungsten carbide, yttria-stabalized zirconia, silicon carbide, and high speed steel. The selection of grinding media depends on the vial material, milling conditions (temperature [94], time, atmosphere, mill type), as well as the amount and chemical composition of impurities that are acceptable. During milling the exposure of new surfaces of the vial and grinding media leads to contamination of the milled powder [95]. Methods to decrease contamination of the milled powder are to re-use the mill vial and grinding media without cleaning, or the coating of the grinding media with the sample to be milled [96, 97], and the use of process control agents or surfactants [92].

The geometry of the grinding media utilized in high energy ball milling can be rodular, spherical, or other. In planetary and ball mill set-ups, rodular shapes have been shown to minimize impurity levels, but increase the overall mill time in mixer mills. Thus in mixer mills spherical media is preferred [92].

2.4.2.2 Milling Atmosphere

High energy ball milling, can be carried out in different atmospheres. Pyrophoric or otherwise reactive materials should be milled in high purity argon or nitrogen atmospheres depending on the material's reactivity with nitrogen [98]. Material that might otherwise be stable in air, may react with the oxygen present in air under high energy ball milling conditions [82].

Certain types of mill vials and setups allow milling to be performed under vacuum. Atmospheres of nitrogen and ammonia have been used to produce nitrides during milling, while milling under partial pressure of hydrogen has been used to produce hydrides [82]. Therefore, to minimize adverse reactions of material, care must be taken in choosing the milling atmosphere. In some milling studies process control agents have been chosen to limit the adhesion of the milled material to the vial and the balls, while also limiting conglomeration of the milled powder. To lower the partial pressure of oxygen in the system, milling may be performed under high vacuum, if the milling set-up allows for it [92].

2.4.2.3 Ball to Powder Ratio

The ratio of the mass of grinding media to mass of material to be milled is an important variable of high energy milling. A rough steadfast rule of 1:10 powder to ball ratio is generally employed. Other powder to ball ratios may be used; however a large powder to ball mass ratio, when using low density milling media, may lead to stagnation conditions during milling. Milling media of heterogeneous sizes have been shown to reduce milling times, but may lead to excess contamination [93].

2.4.3 Amorphization

Amorphization can occur during high energy ball milling of powders. During high energy milling, particles reduce to a critical size, and further input of energy to the powder causes further plastic deformation leading the powder to appear amorphous in X-ray powder diffraction patterns [78, 99]. The determination of amorphization of these powders is not

possible with XRD techniques alone, and if inferred from XRD data it is called ‘X-ray amorphous’ [92].

2.5 Powder Compaction

Compaction is used to create a dense green body for sintering [100]. Compaction can produce net shaping of the powder, allowing for the sintering of finite geometries. Net shaping of powder compacts prior to sintering is needed when utilizing pressureless sintering techniques, where little to no net shaping of the powder occurs during the sintering stage [101]. In Spark Plasma Sintering (SPS), it is sometimes needed to pre-compact the powder in the die. Pre-compaction of the powder in SPS tooling prior to loading into the SPS machine can allow pre-settling of the powder volume while the SPS tooling, before applying the tooling load during SPS operation. When operating SPS under vacuum, pre-compaction can decrease spill-over when the vacuum is applied [101]. Care must be taken when performing compaction. Density gradients may form in short load cycles. Pressure should be relieved from the compaction die slowly so that the green body remains compacted [102-3]. Multiple compaction cycles should be used to minimize density gradients throughout the length of the green body [101, 104].

2.6 Sintering

Sintering is a process in which particles transform into bulk materials through the formation of bonds [105]. Sintering is usually evident at or above approximately one half the absolute melting point of the material [105]. Through the formation of bonds between particles, sintering lowers the surface energy of the particles, and is the driving force for

sintering to occur. [105]. Dominant mass transport mechanisms during sintering are shown pictorially in Figure 2.6.

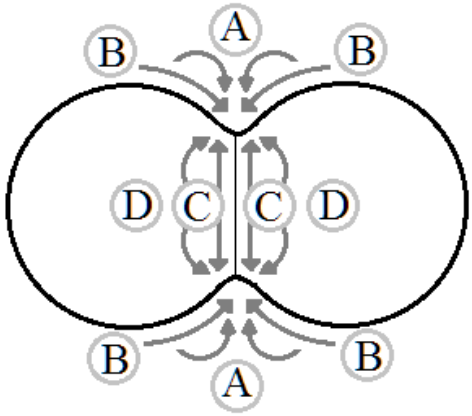

Figure 2.6. Dominant mass transport events during sintering: vaporization and solidification (A), surface diffusion (B), grain boundary diffusion (C), volume diffusion (D).

2.6.1 Spark Plasma Sintering

In Spark Plasma Sintering (SPS), a charge of powder is compressed between graphite punches in a graphite die body. Uniaxial pressure is applied to the graphite punches, compressing the powder charge, to eliminate void spaces within the powder charge [106]. A pulsed DC current is passed through the punches and the compacted powder charge. Joule heating causes the powder to achieve sintering temperatures [107]. A schematic representation is shown in Figure 2.7.

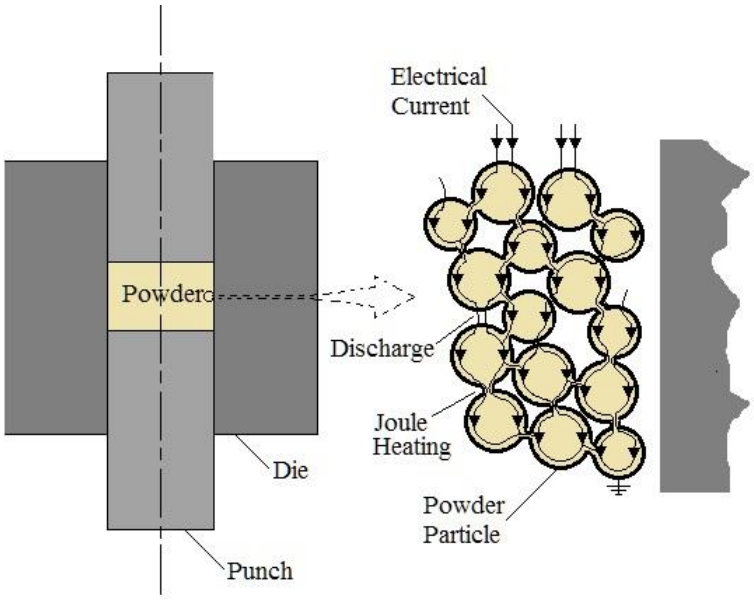

Figure 2.7 SPS punch, die assembly, and Joule heating.

During SPS, the temperature of the die is typically monitored using an external pyrometer or a thermocouple embedded in the die. The internal temperature of the inside of the die can be substantially higher than the temperature that is measured [108]. Finite element analysis studies have been performed to predict the temperature within the powder compact during SPS, and show that conductive powders encapsulated in boron nitride coated graphite lead to higher densification rates [112].

Rapid heating rates during SPS reduce the time that surface diffusion mechanisms are dominant, leading to less exaggerated grain growth than pressureless sintering [109]. The high heating rates lead to rapid densification in short processing times. SPS allows higher densification [110] of transition metal diborides by removing oxide scale on the surface of the powders, and promotion of grain boundary diffusion [108]. Performing SPS under vacuum has also been shown to subsequently remove the boric acid and transition metal oxide films from the transition metal diboride powders during sintering [111].

During SPS, temperature gradients may develop within the SPS tooling. The presence of temperature gradients within the SPS tooling can lead to density gradients within the densified material [112].

2.6.2 Pressureless Sintering

Pressureless sintering is a simple method to produce densified materials. In order to pressureless sinter a material, the material must be compacted into a green body [108]. Pre-compaction is performed to obtain a net-shaped material. The main parameters for pressureless sintering are time and temperature [108].

Sintering of monolithic transition metal borides to full density is difficult due to strong covalent bonding, ultra-high melting points, and low self-diffusion rates [108]. Another cause of difficulty to sintering, is that the surface of transition metal boride powders after milling is often coated with oxides. The presence of boric acid and oxides lead to mass transfer without densification, which occur through vaporization and solidification mechanisms. Transition metal borides must be sintered at temperatures in excess of 1800 ^{o}C to activate grain boundary and volume diffusion mechanisms, which lead to densification. At temperatures lower than 1800 ^{o}C surface diffusion is dominant and does not lead to densification, but grain growth [108].

During pressureless sintering, sintering additives are necessary to produce near full densities of transition metal diboride powders. Sintering additives may form a liquid, allowing for higher densification rates through liquid phase sintering [108]. High energy ball milling of transition metal diborides have been shown to increase densification rates by increasing defect concentrations within the milled powder [108].

2.6.3 Uniaxial Hot Pressing

Uniaxial hot pressing is a pressure-assisted sintering technique that utilizes uniaxial pressure and heat input to activate hard to sinter materials. The die body is typically heated with carbon electrodes and uniaxial pressure is applied to both punches using hydraulics [108]. A schematic of uniaxial hot pressing is shown in Figure 2.8.

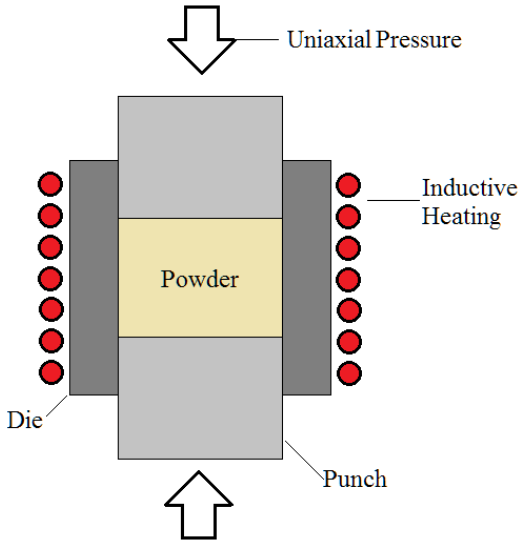

Figure 2.8. Diagram of uniaxial hotpressing.

Uniaxial hot pressing is typically carried out under vacuum or in an inert atmosphere. The uniaxial pressure is applied after the apparatus comes to final temperature to allow for expansion of the tooling. A pressure approximately 35 MPa is applied on the top and bottom punch. Sintering parameters include: time, temperature, pressure, atmosphere, material loading volume and initial particle sizes. Uniaxial hot pressing is confined to simple shapes and geometries, cylindrical being the easiest to perform [108].

3. Experimental

3.1 Preliminary Experimental Procedure

The experimental procedure for the preliminary experiments followed a similar procedure for that of the SPS experiments. When the experimental procedure of the preliminary experiments deviate from that of the SPS experiments, it is discussed in its respective results section.

When performing compaction of powders to a green body for pressureless sintering, a BenchPress™ 3628 (Spex SamplePrep, Metuchen, NJ) was used. The BenchPress™ is a pneumatic press and is shown in Figure 3.1.

Figure 3.1 BenchPress™ 3628 pneumatic press

Green pellets of mechanically alloyed boride based composites were formed using a 8mm diameter die and punch assembly, shown in Figure 3.2. Before assembly, the base, die

body, die, and a hardened steel pellet were coated in a light coating of PTFE based release spray (Allied High Tech Products, Inc.). The PTFE release spray was found to be essential to prevent sticking and damaging of the die body.

To assemble die for pressing, the die body was placed over the base and a hardened steel pellet was inserted into the die body. Using the die, the hardened steel pellet was coercered to the base of the die body. Now, enough mechanically alloyed boride based composite powder was loaded into the die to form a 4 mm tall pellet at 50% of the theoretical density of the powder. The die was slowly inserted into the die body to avoid powder loss. The die was compressed by hand before loading into the BenchPress™. A load of 1.06 GPa was applied quickly to allow the powder to settle and eliminate any voids. The load was held for 60 s. The load was slowly and uniformilly released over 60 s to avoid spring back of the powder compact. The compaction cycle was performed up to three times, in efforts to avoid density gradients and pockets [101, 104].

Figure 3.2 Die and punch assembly.

3.2 Spark Plasma Sintering Experimental Procedure

Specific powder batches of ZrB_2, HfB_2, Ta, Zr, Hf, Gd_2O_3, and LaB_6 were procured from Alfa Aesar (Alfa Aesar, Ward Hill, MA). The purity of all as-received powders was ≥ 99.5%, and the size of powder batches except LaB_6 was <44µm.

The powders with nominal compositions of 1:1 HfB_2-ZrB_2, 4:1 HfB_2-ZrB_2, 1:4 HfB_2-ZrB_2, 1:1 HfB_2-ZrB_2+1.8 mol% LaB_6, 1:1 HfB_2-ZrB_2 +1.8 mol % Gd_2O_3 , 1:1 HfB_2-ZrB_2 + Ta (Boron/Metal = 1.86), 1:1 HfB_2-ZrB_2 + Zr (Boron/Metal = 1.86), and 1:1 HfB_2-ZrB_2 + Hf (Boron/Metal = 1.86) were used in this study. Additives were chosen to maintain the P6/mmm hexagonal crystal structure and others increase oxidation resistance [10]. Gd_2O_3 was added to increase oxidation resistance [52]. Ta, Hf, Zr and LaB_6 were added as sintering aids [10, 19, 60]. Elemental additives were added to the base material to bring the boron/metal molar ratios of samples to 1.86 [60].

Table 3.1 lists all the powder batches with their individual identifying names. Samples are labeled according to the nominal composition of constituents. Diboride powder batches containing pyrophoric additives were loaded into the zirconia vial in an inert atmosphere glovebox (M. Braun InertGas-Systeme GmbH, Garching, Germany) and hermetically sealed. The glove box used is shown in Figure 3.3.

Figure 3.3 MBraun Labstar glovebox.

Then high energy ball milling was carried out on these powder batches for 3 h, using a Spex 8000M mixer/mill, shown in Figure 3.4. The powder to ball mass ratio used during the process was 1:10, utilizing yttria-stabilized zirconia (YSZ), spherical grinding media of 6.5 mm diameter (Inframat Advanced Materials LLC, Manchester, CT).

Figure 3.4 SPEX mixer/mill.

SPS was performed using I-85 graphite dies with an inner diameter of 20.6 mm and punches with 20 mm diameter (Electrodes, Inc., USA) in a Dr. Sinter SPS-515S machine (Fuji Electronic Industrial Co., Ltd., Japan). Dr. Sinter SPS-515S machine is shown in Figure 3.5.

Figure 3.5 Dr. Sinter SPS-515S. Located at CAES, Idaho Falls, ID.

The graphite dies were lined with graphite foil. Before loading into the die, the graphite foil was coated in boron nitride (ZYP Coatings, Inc., Oak Ridge, TN), a view of which is shown in Figure 3.6. A heating rate of 100 °C/min was applied during SPS. The SPS tooling was kept under a vacuum of at least 10^{-3} Torr for the entirety of SPS operation. For all runs, 5 kN force was applied to the SPS tooling. Enough powder was added to the graphite dies to yield a 5mm thick disc of each respective composition, a view of which is shown in Figure 3.7.

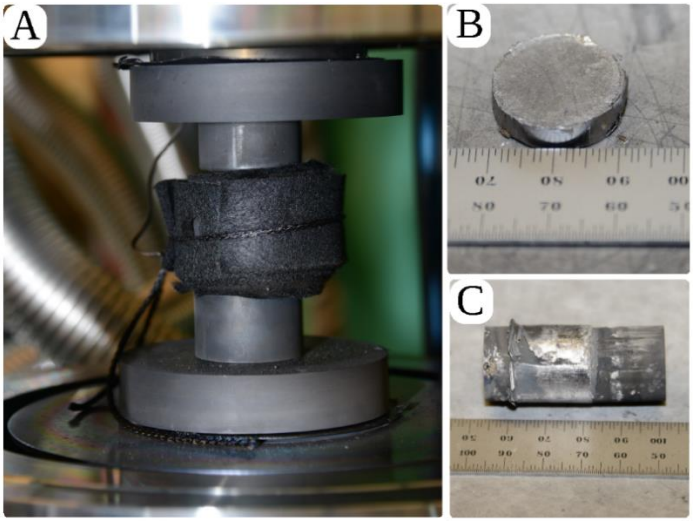

Figure 3.6 The SPS experimental setup for consolidation of mechanically alloyed HfB_2-ZrB_2 solid solution compositions (A). A representative view of the SPSed sample (B). A graphite punch with BN coated graphite foil still covering the SPSed sample (C).

Figure 3.7 Loading I-85 graphite dies for SPS.

Table 1 lists the SPS temperatures and dwell times used in this study. The SPS temperature was 1972 K for all samples and the dwell time for most compositions was 600 s. ZrB_2 and HfB_2 powders were sintered in the as-received state without any ball milling.

Table 3.1 Nomenclature of various powder compositions studied and SPS temperatures and dwell times.

Composition	SPS Temp, K	Hold Time, s
HfB_2	1700	180
ZrB_2	1700	600
$Hf_{0.5}Zr_{0.5}B_2$	1700	600
$Hf_{0.2}Zr_{0.8}B_2$	1700	600
$Hf_{0.8}Zr_{0.2}B_2$	1700	600
$Hf_{0.5}Zr_{0.5}B_2$ + Ta (B/Me = 1.86)	1700	180
$Hf_{0.5}Zr_{0.5}B_2$ + Zr (B/Me = 1.86)	1700	180
$Hf_{0.5}Zr_{0.5}B_2$ + Hf (B/Me = 1.86)	1700	180
$Hf_{0.5}Zr_{0.5}B_2$ + 1.8 mol% LaB_6	1700	300
$Hf_{0.5}Zr_{0.5}B_2$ + 1.8 mol% Gd_2O_3	1700	300

After consolidation, the pellets were initially polished using up to 9 μm Dia-grid grinding discs using a TwinPrep 3™ polishing machine, shown in Figure 3.8. A final polish of 1 μm was performed using a diamond suspension on Velcloth (Allied High Tech Products, Inc.).

Figure 3.8 TwinPrep 3^{TM} polishing machine.

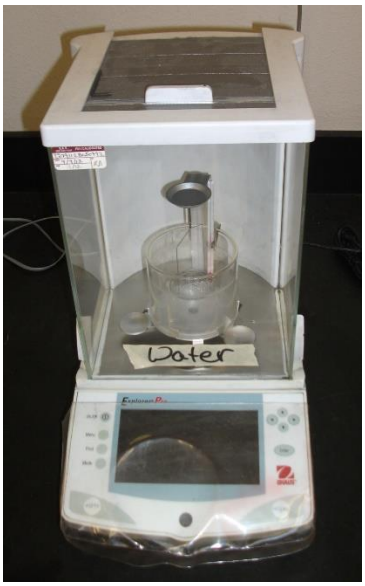

Figure 3.9 Ohaus Explorer Pro.

After polishing to 1µm, the Density (ρ) of the SPSed samples were measured using an Ohaus Explorer Pro (Ohaus Corp., USA) precision digital balance, shown in Figure 3.6. The density measurements were performed in accordance to ASTM B962-08 standard based on the Archimedes principle using the following equation:

$$\rho = \frac{M_{air}}{M_{air} - M_{water}} (\rho_{water} - \rho_{air}) + \rho_{air} \qquad (3.1)$$

Where, M_{air} is the mass of the object in air, M_{water} the mass of the object in water, ρ_{water} the density of water, and ρ_{air} the density of air, which is taken to be 0.0012 g/cm^3.

After polishing to 1µm, the samples were sectioned utilizing a diamond sectioning saw (IsoMet™ 1000, Buehler, Chicago, IL), shown in Figure 3.10. A pie section, consisting of 1/8 of the disc shaped samples was removed.

Figure 3.10 IsoMet™ 1000 precision sectioning saw.

The pie-slice-shaped section, removed from each polished SPS sample, were mounted in a copper-based-conductive mounting powder (Allied High Tech Products, Inc.) so that the radial plane of the section is normal to the surface of the mount, as shown in Figure 3.11. Mounting was performed using a TERAPRESS™ TP-7001 compression mounting press (PACE Technologies®, Tucson, AZ). Figure 3.12 shows the compression mounting press and the copper based mount. Before placing the sectioned sample on the piston of the mounting press, copious amounts of PTFE based release spray (Allied High Tech Products, Inc.) was applied to all working surfaces of the press. The pressure of the mounting press was set to 90

PSI, temperature was set to 190 ºC for a hold time of 9 min. A mounted specimen is shown in Figure 3.11

After mounting, the sections were polished to 0.5 µm using a diamond suspension. The samples were sonicated in DI water for up to 45 s to remove the diamond suspension from the surface pores. After sonication, the samples were dried for up to 2 h in a vacuum chamber.

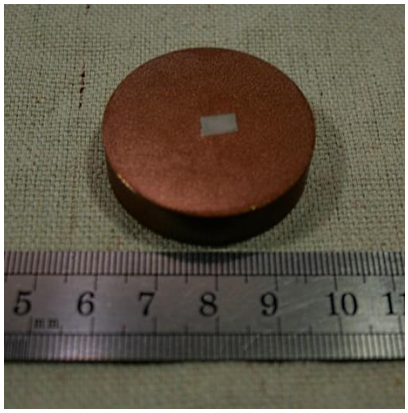

Figure 3.11 Sectioned SPS sample mounted in a copper-based-conductive. The exposed surface of the sample is of the radial plane of the SPS pellet.

Figure 3.12 TERAPRESS™ TP-7001 compression mounting press.

After drying, the samples were loaded into a scanning electron microscope. The field emission scanning electron microscope (FEG-SEM) used was a LEO Supra 35VP (Zeiss, Jena, Germany) and is shown in Figure 3.13. Backscatter electron and secondary electron detectors were used for the breadth of the results.

Figure 3.13 Field Emission Scanning Electron Microscope, LEO Supra 35VP.

X-ray diffraction patterns (XRD) were obtained using a D5000 Diffractometer (Siemens AG, Munich, Germany) at a scan rate of 0.02^{o} and a hold time of 5 s. A photograph of the D5000 used during the study is shown in Figure 3.14. Powder XRD was performed by making a suspension of the powder in ethanol and evenly applying the suspension on the surface of a plane of x-ray glass. Lattice parameters for ZrB_2 and/or HfB_2 based SPSed compositions were calculated from indexed XRD reflections.

Figure 3.14 Seimens D5000 powder X-ray diffractometer.

From indexed planes of hk0 type, Equation 3.2, was used to calculate the lattice parameter 'a', and from indexed planes of 00l type, Equation 3.3, was used to calculate the lattice parameter 'c'.

$$a = \frac{\lambda}{\sqrt{3}sin\theta}\sqrt{h^2 + hk + k^2} \tag{3.2}$$

$$c = \frac{\lambda}{2\,sin\theta}\,l \tag{3.3}$$

Qualitative information about strain and crystallite size was gained from XRD reflections utilizing the Williamson-Hall equation, Equation 3.4.

$$\beta_t\, cos\theta = C\varepsilon sin\theta + \frac{K\lambda}{L} \tag{3.4}$$

Where β_t is the integral breadth of XRD reflections, C and K are constants, L is the crystallite size, θ is the Bragg angle, and ε is the strain. From the Williamson-Hall plots, the y-intercept is inversely proportional to crystallite size, and the slope of the line is proportional to strain.

Electrical resistivity of the SPSed samples were measured from the slope of polarization resistance plot and sample geometry. Polarization resistance data was generated using a two-point probe and an Interface 1000 (Gamry Instruments, Pennsylvania, USA), shown in Figure 3.15.

Figure 3.15 Gamry Instruments Interface™ 1000.

Vickers micro-indentation hardness of the SPSed samples were measured using 1 kg_f (9.81 N) load for 20s dwell time, in a LECO LM100 micro-indentation hardness tester (St. Joseph, Michigan, USA), shown in Figure 3.16. Indentation diagonals and crack lengths (generated at the corners of the square impression) were measured using the FEG-SEM.

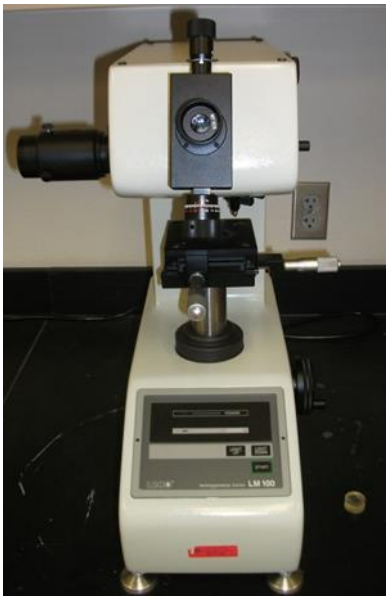

Figure 3.16 LECO LM100 micro-indentation hardness machine.

4. Results & Discussion

4.1 Preliminary Results

In efforts to maximize effectiveness of further experiments, preliminary experiments of HfB_2 and ZrB_2 bearing composites were conducted. This allowed for many findings that aided in prioritizing SPS experiments.

4.1.1 Mechanochemical Synthesis of ZrB_2

Amorphous boron was procured from Alfa Aesar. The purity was ≥ 99.5%, and the size was <44μm. Elemental zirconium received from Alfa Aesar was packaged in water. Proportions of zirconium powder were retrieved from underneath the water. The zirconium powder was loaded into centrifuge tubes and flushed with ethanol. Following several rinsings and centrifuging, the zirconium powder was removed and placed in a petri dish to dry. An assumption was made that the zirconium, having been shipped and stored under water, would have developed a thick enough oxide scale to resist further oxidation in air during the drying time.

After the zirconium was dry, it was loaded into an inert atmosphere glovebox. Within the inert atmosphere glovebox, the amorphous boron and zirconium were loaded into a zirconia vial, in a 2:1 molar ratio. Yttria-stabilized zirconia grinding media (6.5 mm diameter spheres) were added to the vial, and the vial was hermetically sealed.

The hermetically sealed zirconia mill vial was loaded into a Spex mixer mill and milled for 45 m. After milling, the zirconia mill vial was allowed to cool in the mixer mill overnight. Upon cooling, the zirconia mill vial was opened and enough reagent grade ethanol was added to fill the vial halfway. The vial was again hermetically sealed and returned to the mixer mill

for 5 minutes. The contents of the mill vial were strained into a petri dish to dry in a fume hood.

X-ray powder diffraction was performed on the mechanochemically synthesized ZrB_2, as well as ZrB_2 obtained commercially to compare the crystallographic similarities. XRD of the mechanochemically synthesized ZrB_2 revealed reflections corresponding to the p6/mmm hexagonal geometry, and is shown in Figure 4.1. A comparison of mechanochemically synthesized ZrB_2 to commercially available ZrB_2 is shown in Figure 4.1. The presence of a weak reflection at 31° 2θ is due to monoclinic ZrO_2 [38], presumably due to elemental zirconium being stored under water.

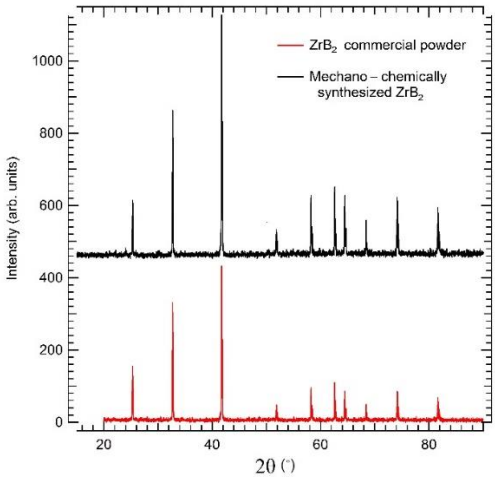

Figure 4.1. X-ray powder diffraction patterns of commercially available ZrB_2 and ZrB_2 synthesized by mechanochemical synthesis.

From the results obtained after mechanochemical synthesis of ZrB_2, it was concluded that commercially available ZrB_2 was chemically equivalent to that of mechanochemically synthesized ZrB_2. In literature, Aviles *et al* demonstrated that ZrB_2 and HfB_2 solid solutions could be formed utilizing elemental synthesis during ball milling [74]. In subsequent studies,

commercially available ZrB_2 and HfB_2 were utilized as starting reagents for solid solution formation.

4.1.2 Mechanically Alloyed Solid Solutions

Molar ratios of 1:1 ZrB_2 and HfB_2 were added to a stainless steel milling vial as a 5 gram load. Stainless steel grinding media (~5mm spheres) were added to the milling vial as a 1:20 powder to ball mass ratio.

The stainless steel milling vial was loaded into a Spex mixer mill, and the powder mixture was milled for 5, 60, 180, and 270 minutes. Milling was halted and less than 100 mg of powder removed after each of the times specified above. After which the milling resumed.

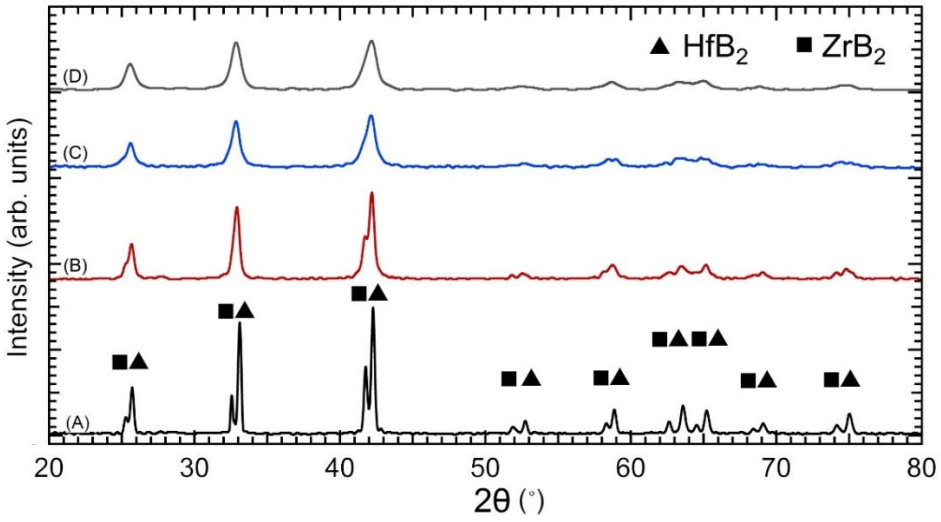

Figure 4.2. X-ray powder diffraction patterns of the products of mechanically alloying a 1:1 mixture of HfB_2-ZrB_2, powder to ball ratio is 1:20: 5 minutes (A), 60 minutes (B), 180 minutes (C), 270 minutes (D).

XRD patterns were obtained after each subsequent milling time to track the progress of mechanical alloying of 1:1 ZrB_2-HfB_2. Figure 4.2 shows the XRD pattern of each milling

time, offset from one another on the same plot for clarity. After 180 min, it is seen that higher angle reflections become x-ray amorphous, and lower angle reflections tend towards a position between that of ZrB_2 and HfB_2. The position of XRD reflections was thought to signify that a solid solution of $Zr_{0.5}Hf_{0.5}B_2$ was formed. The solid state mechanical alloying of ZrB_2 - HfB_2 solid solutions from starting diborides in this study, is possibly the first in available literature.

4.1.3 Pressureless-Sintering of Solid Solutions

$Zr_{0.5}Hf_{0.5}B_2$ mechanically alloyed powder was pressed into 8 mm diameter, 4 mm long pellets, at 1.06 GPa. As pressed pellets were characterized using a FEG-SEM. Secondary electron imaging was used to image the pellets and are shown in Figure 4.3.

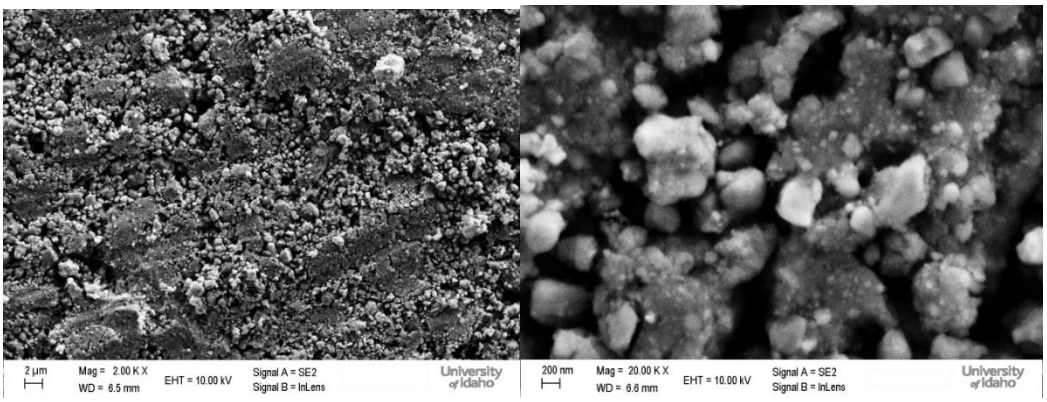

Figure 4.3: Secondary electron image of (1:1) Hafnium diboride, zirconium diboride solid solution pressed pellets. (left) imaged at 2Kx magnification shows surface porosity up to 2 µm in diameter. (right) imaged at 20Kx shows Hafnium diboride, zirconium diboride solid.

Density gradients can be seen as stripes on the material surface. The morphology of the hafnium diboride, zirconium diboride solid solution pellets were found to be porous in nature. Energy dispersive spectroscopy (EDS) of the pressed pellet showed hafnium diboride and zirconium diboride to be intricately mixed. The pressure used to compact the pellets was

the maximum pressure for the die used. The application of a cyclic loading of the powder charge in the die, led to higher green densities of the pellets [104].

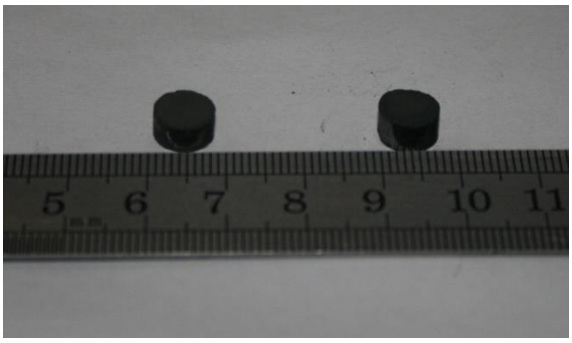

Figure 4.4 As-Pressed (1:1) Hafnium diboride, zirconium diboride solid solution pressed pellets.

After compaction, the pressed pellets were sintered in an alumina boat, at 1700^{0}C for three hours in a tube furnace. The ramp rate of the tube furnace was 8^{0}C min^{-1} and the tube furnace was continually purged with high purity argon, at a flow rate of 3 SCFH at 30PSI. Based on the dimensions of the tube furnace, 3 SCFH flow rate was determined satisfactory for an inert atmosphere within the furnace [108]. Secondary Electron imaging and EDS of the pressureless sintered hafnium diboride, zirconium diboride solid solution is in figure 4.5. The light regions are sintered hafnium diboride, zirconium diboride solid solution, the darkest regions are porosity. Analysis using EDS determined the dark grey regions are laden with aluminum and oxygen contaminants.

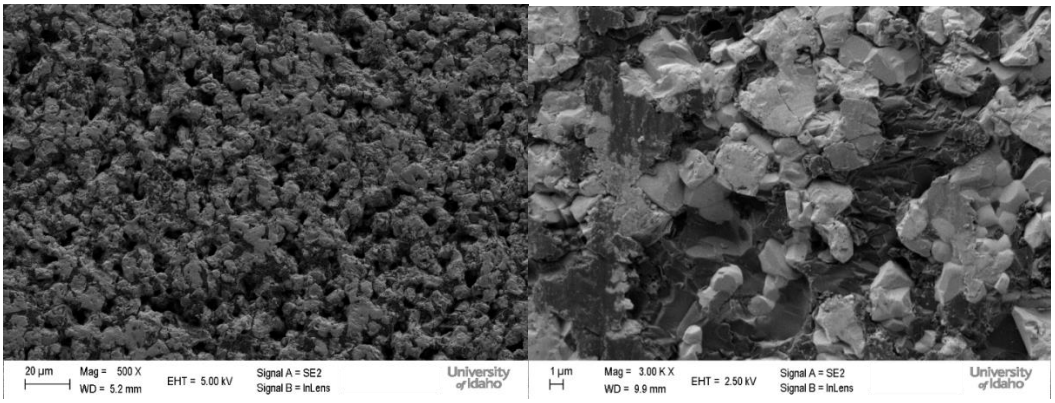

Figure 4.5 Secondary imaging of the sintered polished (1:1) Hafnium diboride, zirconium diboride solid solution pellet as polished.

The sintered pellet was determined to contain aluminum and oxygen contaminates, presumably from the boat and possibly from the high purity argon. The sintered pellet was cut along the longitudinal plane of the cylindrical pellet using a precision sectioning diamond saw, to allow characterization of the depth of the aluminum and oxygen impurities. After sectioning, the pellet was sonicated for up to 120 s in ethanol, followed by a DI water rinse and further sonication in DI water for 120 s. The sonication was needed to eliminate unwanted water-based cutting lubricant from the surface and surface connected pores of the pellet [11]. After sonication, the pellet was dried in a vacuum chamber for 2 h prior to loading into the SEM, to remove any residual water [11]. The cut sample was oriented with the sectioned planar surface normal to the electron gun of the SEM. The cut pellet was examined using a line scan EDS.

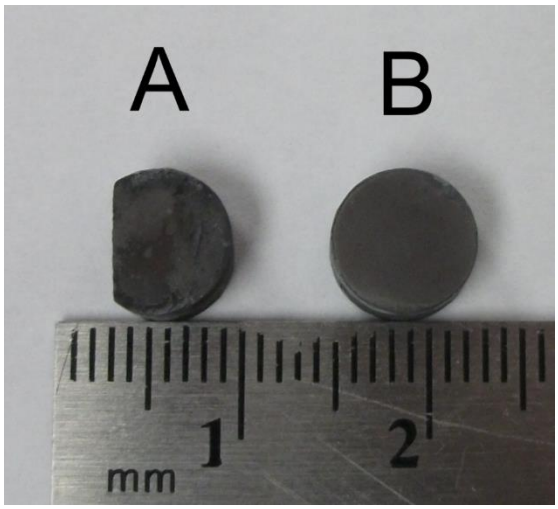

Figure 4.6 macroscopic view of $Zr_{0.5}Hf_{0.5}B_2$ sintered pellets. Sample planed along longitudinal direction (A), and Sintered pellet (B).

The line scan was taken from the edge of the pellet to the center region of the pellet along the transverse direction. During EDS, An accelerating voltage of 2.5kV was used to aid in determination of aluminum and oxygen contaminates. Voltages beyond 2.5kV had a detrimental bremsstrahlung spectrum superimposed on the line scan, which made quantification more difficult. A low accelerating voltage made difficult the determination of the Hf and Zr content in the pellet during the line scan EDS. The resulting line scan spectrum and accompanying image is shown in Figure 4.7.

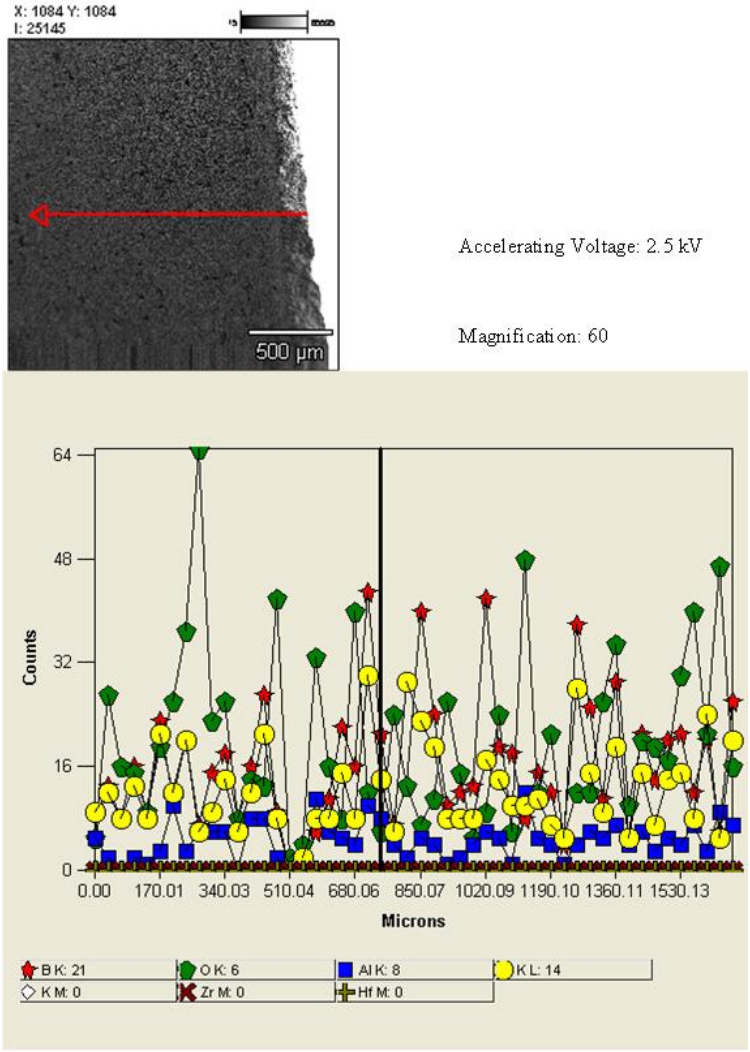

Figure 4.7: EDS line scan of polished (1:1) hafnium diboride, zirconium diboride solid solution sintered pellet that had been cut along the longitudinal plane of the pellet.

Aluminum content of the pellet was seen to remain relatively constant throughout the 1.53 mm scan depth. Oxygen contamination had a peak concentration around 0.2 mm from the edge. To determine whether the presence of aluminum and oxygen contamination negatively influenced the crystallographic parameters of the ZrB_2-HfB_2 solid solution, XRD was performed on the planed surface of the pressureless sintered pellet, and is shown in Figure 4.8. The XRD pattern of the sintered pellet is shown stacked on top of the XRD pattern of commercially available ZrB_2 and HfB_2 that were used to mechanically alloy the HfB_2-ZrB_2

solid solution powder. The XRD pattern of the HfB_2-ZrB_2 solid solution sintered pellet is shown to have retained the crystallographic bonding of the HfB_2-ZrB_2 solid solution despite the aluminum and oxygen contamination. The presence of aluminum and oxide phases are clearly evident in the forms of weak reflections in the XRD pattern.

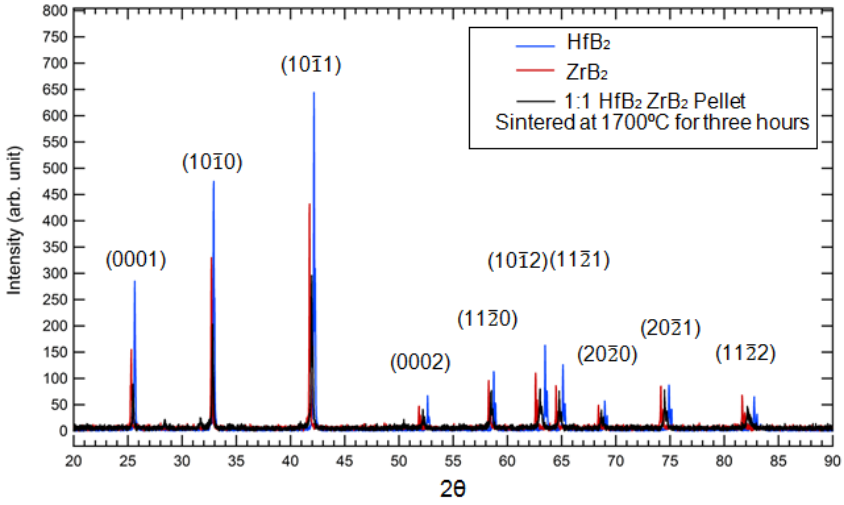

Figure 4.8: XRD pattern of (1:1) hafnium diboride, zirconium diboride solid solution sintered pellet. The XRD pattern confirmed the formation of P6/mmm hexagonal diboride phases.

It has been shown that despite the large contamination level in the pressureless-sintered HfB_2-ZrB_2 solid solution, the corresponding P6/mmm hexagonal symmetry, specifically of $Zr_{05}Hf_{0.5}B_2$ solid solutions, is still maintained. It is thought that the weak reflections at 28º and 32º 2θ correspond to monoclinic HfO_2 and ZrO_2 phases [38].

In order to determine the progress of the sintering, density measurements of the as-pressed and sintered hafnium diboride, zirconium diboride solid solution pellets were performed. Density measurements are shown in Table 4.1. Theoretical density was calculated based on the density calculated by the rule of mixtures for nominally pure HfB_2-ZrB_2 [11].

The density of the as-pressed pellet was seen to be 39% of the theoretical density of that of nominally pure HfB_2-ZrB_2.

Table 4.1 Physical dimensions of specimens and density values measured using Archimedes' technique.

Sample Id	Area (m^2)	Length (m)	$Mass_{air}$ (g)	$Mass_{water}$ (g)	ρ_{Water} (g cm^{-3})	ρ_{pellet} (g cm^{-3})	Theroretical Density
As pressed	$4.75x10^{-5}$	$4.44x10^{-3}$	0.8850	0.6124	0.99777	3.24	39%
Sintered	$5.09x10^{-5}$	$5.06x10^{-3}$	1.1973	0.9944	0.99799	5.88	71%

The pressureless sintered HfB_2-ZrB_2 solid solution pellet underwent dimensional changes during sintering [26]. It is presumed that during sintering, an aluminum and potassium based glaze, on the alumina boat, began to melt during sintering of the pellet and infused into the porous network of the diboride pellet. The resulting infusion of the glaze and subsequent oxidation caused the pellet to swell past its as-pressed dimensions.

In order to quantify the electrical resistivity of the as-pressed and pressureless sintered sample, a two point probe was assembled from copper paddles. The samples were placed between the copper paddles and approximately 2.5 MPa was applied, sandwiching the pellets between the copper paddles. Polarization resistance data was generated utilizing the two point probe. From the slope of the polarization resistance curve, Figure 4.9, resistivity of the pellets were obtained. Qualitatively, it is seen that the resistivity of the pellet decreased significantly after sintering, as is indicated in literature [10]. The decrease in resistivity of the HfB_2-ZrB_2 solid solution pellet after sintering was likely due to the reduction of porosity.

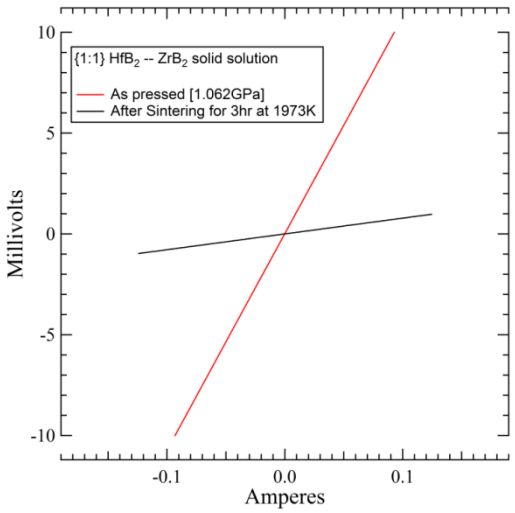

Figure 4.9. Linear polarization data used to generate resistance values for (1:1) HfB_2-ZrB_2 sintered pellets and as-pressed pellets.

The electrical resistance values for the as-pressed and pressureless sintered HfB_2-ZrB_2 solid solution pellets were obtained from the resistivity values and the geometry of the pellets using Equation 4.2.

$$\rho = \frac{AR}{L} \qquad 4.2$$

where ρ is the resistivity, A is the cross sectional area, R is the resistance determined from the slope of Figure 4.9, and L is the length of the cylindrical pellet [11].

To calibrate the polarization resistance technique and to account for possible contact resistance of the pellets surface and the copper paddles of the two point probe, a fit was obtained by performing polarization resistance data for a nominally pure, nearly dense sample of HfB_2 with an equivalent geometry. The corresponding fit was determined to be 147.08 μΩ-cm.

After applying the calibration fit, the resistivity is shown in Table 4.2. The resistivity of the pressureless sintered HfB_2-ZrB_2 solid solution pellets was higher than that of nearly

dense, nominally pure HfB_2 and nearly dense, nominally pure ZrB_2, 8.9 μΩ-cm and 6.71 μΩ-cm, respectively [10].

Table 4.2 Physical dimensions, measured resistance, and calibrated resistivity values for HfB_2-ZrB_2 solid solution pellets.

Sample ID	Resistivity (μΩ-cm)	Resistance (Ω)	Area (m^2)	Length (m)
As pressed	2162.0	127.85	4.75×10^{-5}	4.44×10^{-3}
Sintered	15.6	1.05×10^{-1}	5.09×10^{-5}	5.06×10^{-3}

The sintered pellet was determined to contain significant aluminum and oxygen contaminants. The aluminum contaminants were likely to have come from the sintering boat. The oxygen contaminants were thought to have come from the sintering boat; however, based on the quantity of oxygen contamination in the pellet, it is more likely that the oxygen came from the high-purity argon used while sintering the pellet.

In future experiments in order to alleviate contamination of pressureless sintered pellets, it is desirable to employ an oxygen scrubber to reduce the O_2 content of the high-purity argon from ppm levels down to ppb levels [18]. A nominally pure zirconia sintering boat was procured for future pressureless sintering experiments to minimize contamination levels arising from the sintering conditions. The stainless steel vial used during the mechanochemical synthesis of HfB_2-ZrB_2 was not used during any future milling experiments, in efforts to reduce the quantities of contamination [78], as well as, the contaminating materials.

Yttria-stabilized zirconia spherical grinding media were obtained by Inframet® advanced Materials™ in 6.5 mm diameter and 10 mm diameter spheres for future milling

studies. A zirconia mill vial was procured from SPEX. The zirconia grinding media is less dense than the stainless steel milling media, which may lengthen milling times.

4.1.4 Anodization of 1:1 HfB_2-ZrB_2 +20 vol% SiC +1.8mol % LaB_6

In efforts to determine the viability of 1:1 HfB_2-ZrB_2 +20 vol% SiC +1.8mol % LaB_6 as an electrode material, specific powder batches of SiC and LaB_6 were procured from Alfa Aesar. The purity of all as-received powders was ≥ 99.5%, and the size of powder was 7 µm and -<44µm, for SiC and LaB_6 respectively. 1:1 molar ratio HfB_2 and ZrB_2 were added to a zirconia mill vial, and 1.8 mol% of LaB_6 and 1.8 mol% SiC were added so that the total mass of all the powders in the vial was 5 g.

A powder to ball mass ratio of 1:10 was utilized in efforts to minimize the overall contamination of the mixture. The powders were mechanically alloyed in a SPEX mixer/mill for 3 h, utilizing yttria-stabilized zirconia grinding media (6.5 mm diameter spheres). After milling, enough ethanol was added to the mill vial to fill the vial halfway. The milling vial and contents were returned to the mill for 5 min. Upon which, the contents of the mill vial were strained into a petri dish and placed into an isolated fume hood for 2 days to dry. Sufficient mechanically alloyed powder was added to an 8 mm diameter powder compaction die to form approximately a 4 mm tall cylindrical pellet cyclic loaded at 1.06 GPa.

Upon compaction, the pellets were placed in a zirconia sintering boat and loaded into an inert atmosphere tube furnace. The inert atmosphere tube furnace was continually purged with ultra-high purity argon (ppb oxygen levels) at 30 PSI and 5 SCFH. The ramp rate of the furnace was 3.5 $^{o}C\ min^{-1}$ with an 80 min hold at 1220 ^{o}C to allow for the monoclinic to

tetragonal phase transition of the ZrO_2 boat [26]. The furnace was programmed to hold at 1700 ºC for 3 h.

After sintering, the pellet was ground utilizing various SiC grinding papers, followed by polishing by diamond suspensions on a polishing cloth down to 1 μm finish. After polishing, the pellet was sonicated in DI water to remove any diamond that was caught in the surface pores of the pellet. The pellet was then dried under vacuum for 2 h and loaded into a FEG-SEM. The resulting microstructure, visible due to electron channeling contrast, is shown in Figure 4.10. From Figure 4.10, it can been seen that final stages of sintering were not accomplished [44].

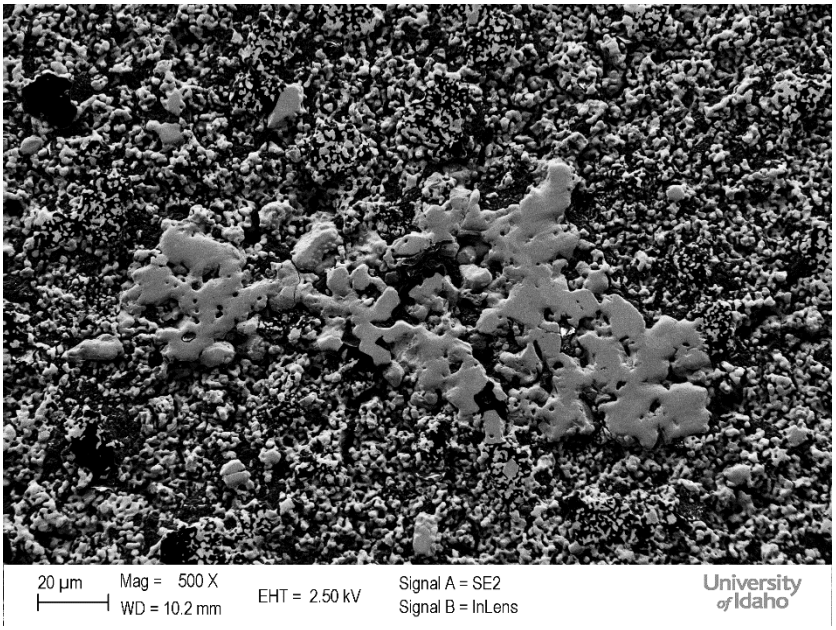

Figure 4.10. 1:1 HfB_2-ZrB_2 +20 vol% SiC +1.8mol % LaB_6 sintered at 1700^0C for 3 h.

After sintering, a 2 mm diameter hole was drilled in the edge of the 1:1 HfB_2-ZrB_2 + 20 vol% SiC + 1.8mol % LaB_6 pellet, deep enough to make sufficient mechanical connection

with a 12 AWG copper wire. The tip of the 12 AWG shielded copper wire was exposed and press fit into the hole. Adequate layers of enamel was applied to make the union of the pellet and wire watertight. The connection of the copper wire and the pellet were sealed to minimize the presence of copper ions in the solution during anodization. A 0.1 M solution of NH_4F was prepared as the reagent. NH_4F was chosen to chemically attach the boron, allowing a TM oxide to form as a coating.

The pellet and a platinum flag, with approximately 4.5 cm^2 surface area, were lowered into the 0.1 M NH_4F solution, maintaining a mean separation of 10 mm. The pellet and the platinum flag were energized using a constant voltage power supply at 40 V for 1 h. During anodization, the current was seen to increase and a film developed at the bottom of the solution, signifying that the resulting oxide layer was not stable.

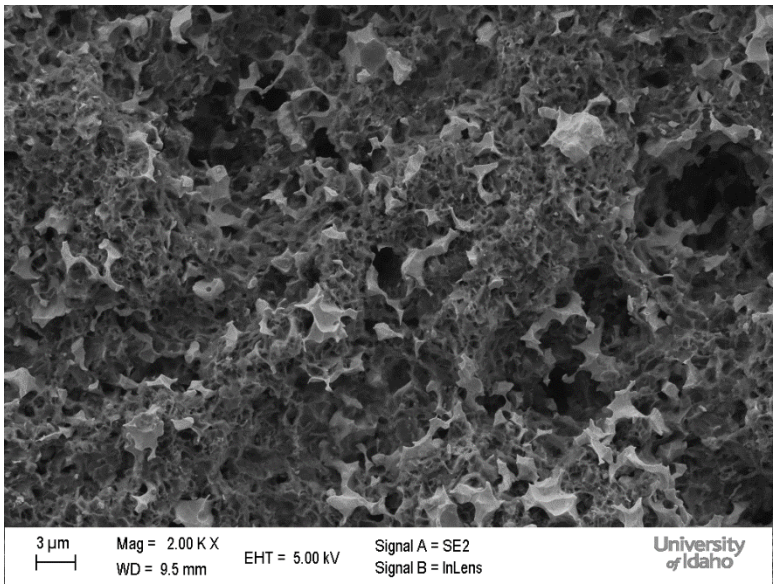

Figure 4.11. Sintered 1:1 HfB_2-ZrB_2 +20 vol% SiC +1.8mol % LaB_6 was anodized for 1 h at 40V in 0.1M NH4F using a platinum flag as a counter electrode. Mean separation between sample and flag was 10 mm.

After anodization, the copper wire and enamel were carefully removed mechanically from the pellet. The pellet was rinsed in DI water and allowed to dry under vacuum for 2 h before loading into the FEG-SEM and imaged, shown in Figure 4.11. Anodization of the sintered 1:1 HfB_2-ZrB_2 + 20 vol% SiC +1.8 mol % LaB_6 pellet destroyed the microstructure, as compared to Figure 4.10. It can be seen, in Figure 4.11, that a porous-in-nature oxide film was developed on the surface of the pellet.

To test the effect of anodization on the oxidation properties of sintered 1:1 HfB_2-ZrB_2 +20 vol% SiC +1.8mol % LaB_6, an as-sintered and an anodized, sintered pellet were loaded into a tube furnace in air. The tube furnace was heated with a ramp rate of 5 $^oC\ min^{-1}$ to a final temperature of 1700 ^oC. The temperature held at 1700 ^oC for 1 h. The pellets were exposed to air during the heating, dwell, and cooling times to simulate a shutdown operation at a MHD direct power extraction facility. From visual inspection, both pellets completely oxidized during the oxidation test.

After each stage of the test, XRD was performed to track the crystallographic changes that occurred. Figure 4.12 shows the XRD pattern for as-sintered, post-anodization and subsequent oxidation of the anodized pellet. It is noted that the presence of weak reflections in the as-sintered XRD pattern are absent in the anodized XRD pattern. It is plausible that during anodization secondary oxide phases were stripped from the pellet, becoming the film at the bottom of the anodization solution; however, the chemical composition of the film was not obtained. After oxidation, no diboride phases can be detected in the XRD pattern, suggesting that the pellets were effectively oxidized during the study. The porous oxide film developed on the surface of the 1:1 HfB_2-ZrB_2 + 20 vol% SiC +1.8mol% LaB_6 pellet after anodization provided little to no oxidation resistance during oxidation.

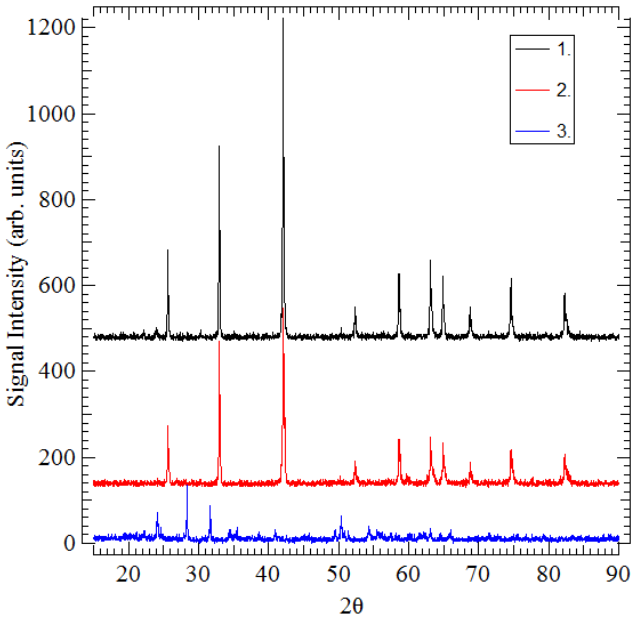

Figure 4.12. XRD patterns: 1.) 1:1 HfB_2-ZrB_2 +20 vol% SiC +1.8mol % LaB_6 sintered at 1700^{0}C for 3 hours in a zirconia boat under an argon atmosphere (< 2ppb O_2). 2.) Sample was then anodized for 1 h at 40V in 0.1M NH4F using a platinum flag as a counter electrode. Mean separation between sample and flag was 10mm. 3.) Sample was then oxidized at 1700 ^{0}C for 1hr in air.

From the results of this experiment, it cannot be confirmed that anodization does not improve oxidation resistance during brief periods of high temperature atmosphere exposure. During the experiment detailed in this section, it is presumed that the sample was exposed to superheated air for up to 8 h during the heating, hold, and cooling cycle. The long exposure to superheated air, oxidized the samples completely, and the oxidation rate of the samples could not be obtained.

4.2 Characterization of Mechanical Alloyed $Hf_xZr_{(1-x)}B_2$ ($0.2 \leq x \leq 0.8$) Solid Solutions Consolidated by Spark Plasma Sintering.

SPSed $Hf_xZr_{(1-x)}B_2$ ($0.2 \leq x \leq 0.8$) Solid Solutions were studied for various phase content, relevant crystallographic parameters, room temperature electrical resistivity,

hardness, and density. An image of a SPSed pellet after removal from the SPS tooling is shown in Figure 4.13.

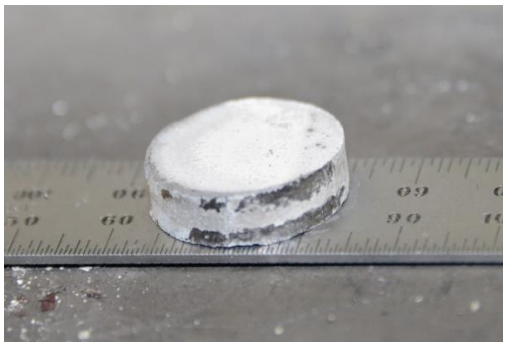

Figure 4.13 ZrB_2 pellet after removal from the SPS tooling. Pellet is covered with BN that adhered to the pellet from the coating on the graphite foil.

Table 4.3 summarizes the physical density, hardness, planar porosity, and electrical resistivity of SPSed materials measured at room temperature. Theoretical density of the samples was calculated by the rule of mixture. Percent theoretical density (TD) was calculated as the ratio of the observed density and the calculated theoretical density. The discrepancy between percent porosity and TD is likely due to non-boride phases, which are evidenced in XRD data as weak reflections at 28° and 31.5° 2θ, respectively. Which is thought to be monoclinic ZrB_2 and HfB_2 [38].

Table 4.3 Spark plasma sintering conditions and relevant properties.

Sample Composition	Relative Density (%)	Hardness (GPa)	Electrical Resistivity (μΩ-cm)	Grain Size (μm)	% Porosity
HfB_2	91.4	20.07	9.2	3.6 ± 1.6	10.6
ZrB_2	87.2	12.86	6.8	3.1 ± 1.8	20.3
$Hf_{0.5}Zr_{0.5}B_2$	76.2	7.50	5.4	3.3 ± 2.1	26.7
$Hf_{0.2}Zr_{0.8}B_2$	82.9	3.13	6.0	2.3 ± 1.4	19.9
$Hf_{0.8}Zr_{0.2}B_2$	76.5	8.32	9.3	3.7 ± 1.6	20.0

EDS analysis of SPSed materials detected carbon and oxygen impurities. The weak reflections of non-boride phases, likely monoclinic ZrO_2 and HfO_2, are strongest in the XRD patterns of milled powders. Because all SPS runs were carried out utilizing identical atmospheres, the detection of monoclinic ZrO_2 and HfO_2 in the XRD patterns of milled powders, is likely due to HfB_2 and ZrB_2 reacting with air during high energy ball milling. The existence of non-boride phases in the milled powder for SPS is thought to have limited densification, as reported in literature [46].

SPSed as-received materials exhibited higher Vickers hardness compared to the mechanically alloyed materials, likely due to the non-boride phases present before SPS. Hardness values ranged from HfB_2 as the highest to $Hf_{0.2}Zr_{0.8}B_2$ as the lowest. A clear correlation between TD and Vickers hardness of SPSed materials is not evident. Despite the varying hardness, electrical resistivity and TD between the SPSed mechanical alloyed mixtures of HfB_2 and ZrB_2, grain size is comparatively uniform. $Hf_{0.8}Zr_{0.2}B_2$ displayed the highest overall electrical resistivity, largest grain size, and second lowest achieved TD.

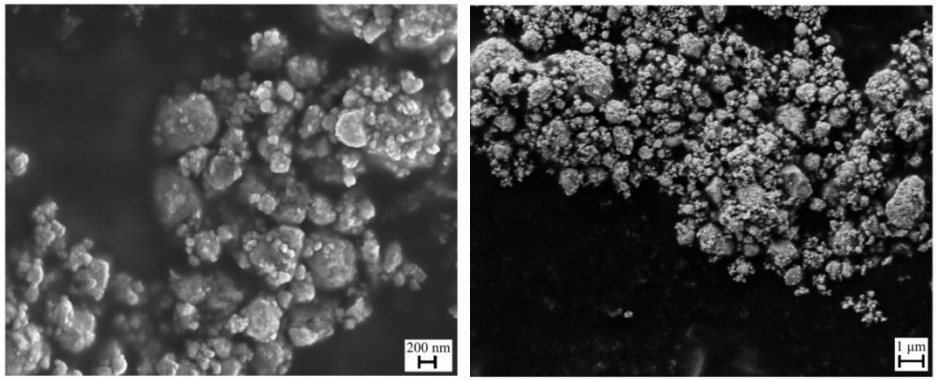

Figure 4.14. FE-SEM micrographs of mechanically alloyed $Hf_{0.5}Zr_{0.5}B_2$ powder.

Mechanically alloyed powder exhibited aggregate particles with an aggregate size in the range of 1-5 µm. The aggregate particles consisted of nanoparticles. Figure 4.14 shows

FEG-SEM micrographs of mechanically alloyed $Hf_{0.5}Zr_{0.5}B_2$ powder prior to sintering. Nano-particulate are clearly evident in the aggregate particles.

Low magnification FEG-SEM micrographs of SPSed materials are shown in Figure 4.15. Pores in the HfB_2 micrograph indicated that the final stage of densification was not reached in the 180 s SPS dwell time. It is possible that full densification of HfB_2 could be possible if the dwell time were increased drastically [10].

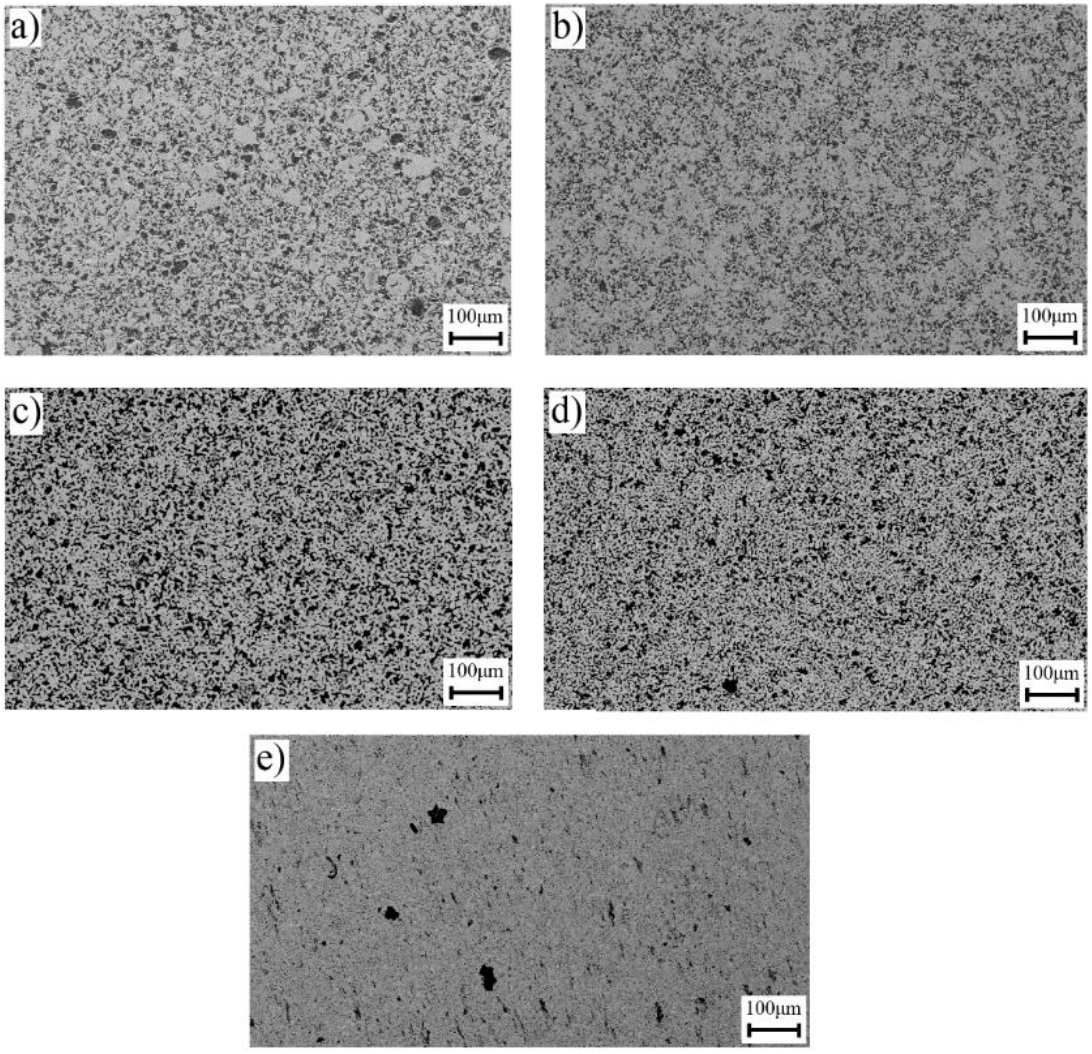

Figure 4.15. Low magnification FE-SEM micrographs of SPSed ZrB_2 (a), $Hf_{0.8}Zr_{0.2}B_2$ (b), $Hf_{0.5}Zr_{0.5}B_2$ (c), $Hf_{0.2}Zr_{0.8}B_2$ (d), and HfB_2 (e).

Grain size distributions for SPSed materials are shown in Figure 4.16. The grain size distributions were generated utilizing electron channeling contrast seen in back-scatter electron mode of a FEG-SEM. Grain size distrubutions were calculated from grain size measurements using Image J [113]. HfB_2 and $Hf_{0.8}Zr_{0.2}B_2$ exhibit bimodal distributions [11] of grain sizes. The grain size distribution for $Hf_{0.5}Zr_{0.5}B_2$ is multimodal. Qualitatively, grain size distribution for $Hf_{0.8}Zr_{0.2}B_2$, $Hf_{0.5}Zr_{0.5}B_2$, and $Hf_{0.2}Zr_{0.8}B_2$ appear to be the superposition of the grain size distribution for HfB_2 and ZrB_2, with the grain size distributions scaled by the mole ratio of each constituent present. HfB_2 exhibited the largest grain size, while $Hf_{0.5}Zr_{0.5}B_2$ had the smallest grain sizes. The large grain sizes present is SPSed HfB_2 are due to grain coarsening during SPS [38]. HfB_2 was SPSed for 30% less time than that of ZrB_2 or $Hf_xZr_{(1-x)}B_2$ solid solutions.

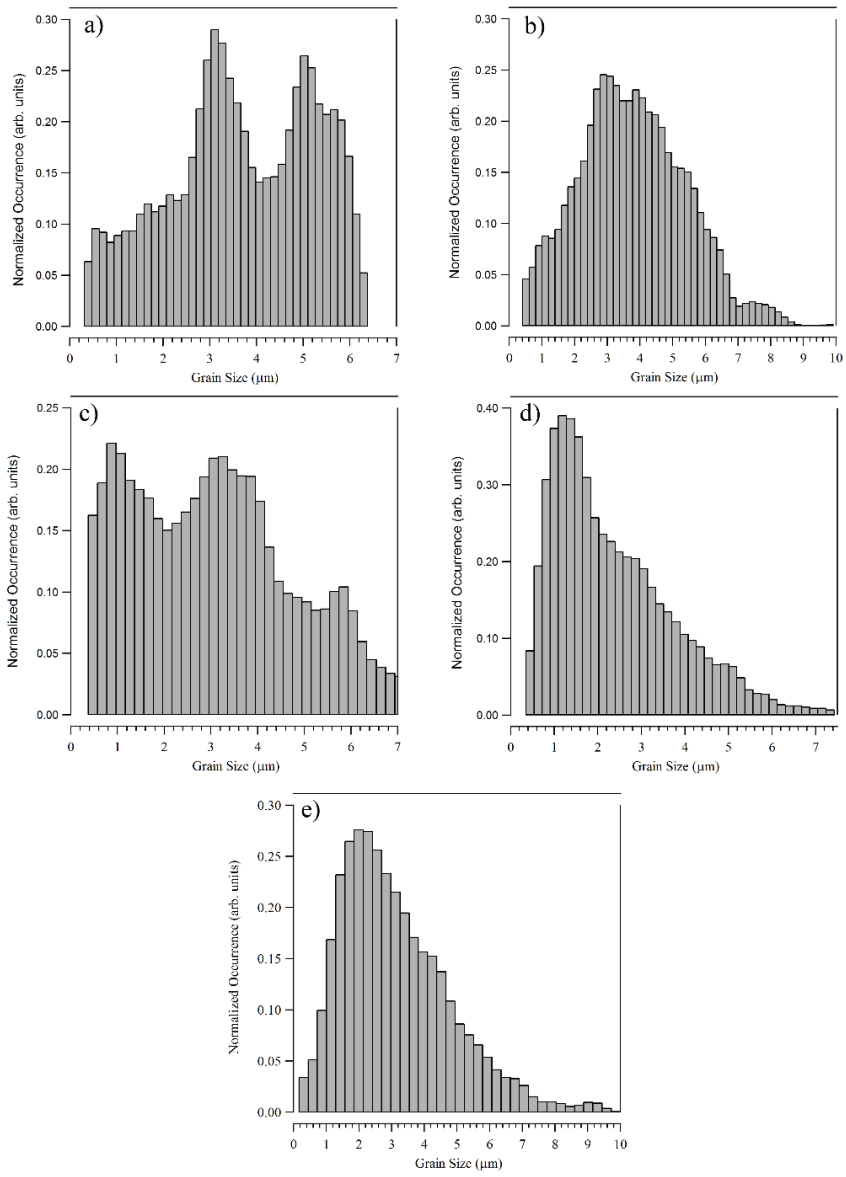

Figure 4.16 Grain size distributions for SPSed samples, generated from grain size measurements with FE-SEM BSE, HfB_2 (a), $Hf_{0.8}Zr_{0.2}B_2$ (b), $Hf_{0.5}Zr_{0.5}B_2$ (c), $Hf_{0.2}Zr_{0.8}B_2$ (d), ZrB_2 (e).

Owing to the crystallographic similarities between ZrB_2 and HfB_2, the lattice constants of mixtures follow a linear Vegard's law relationship. Shown in Table 4.4 are the experimentally obtained lattice parameters. Figure 4.17 shows the lattice constants '*a*' and '*c*' generated experimentally and compared to Vegard's law calculations. It is clear that as the

mole ratio of any constituent is increased, the XRD reflections shifts in the direction of the largest constituent component. The shift of the XRD reflections is proportional to that of the molar ratio of the largest component. $Hf_xZr_{(1-x)}B_2$ solid solutions can be seen to follow a linear Vegard's law relationship for $0.2 \leq x \leq 0.8$.

Table 4.4 Lattice parameters for $Hf_xZr_{(1-x)}B_2$ solid solutions.

Sample Identifier	Lattice Parameter, *a* (*Å*)	Lattice Parameter, *c* (*Å*)
HfB_2	3.133	3.463
ZrB_2	3.159	3.517
$Hf_{0.5}Zr_{0.5}B_2$	3.147	3.491
$Hf_{0.2}Zr_{0.8}B_2$	3.154	3.505
$Hf_{0.8}Zr_{0.2}B_2$	3.139	3.476

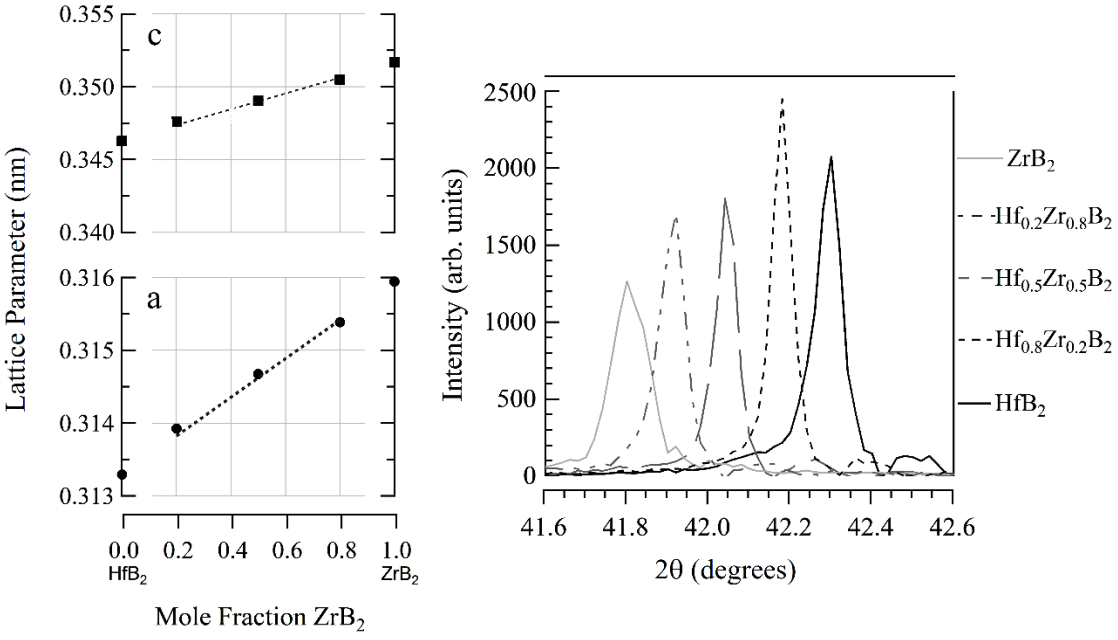

Figure 4.17 The Vegard law relation of calculated and measured lattice parameters for $Hf_xZr_{(1-X)}B_2$ Solid solutions formed during SPS. The black squares and circles are measured lattice parameters. The dotted lines show lattice parameters calculated from Vegard's law relationship. The included XRD patterns, (101) reflection, shows the evolution of the lattice parameter for $Hf_xZr_{(1-X)}B_2$.

Qualitative information about strain and crystallite size can be gained from the Williamson-Hall equation [11]. In Figure 4.18, the Williamson-hall plots are shown for mechanically alloyed powders. It can be noted that $Hf_{0.2}Zr_{0.8}B_2$ has the smallest crystallite size of the mechanically alloyed powders, and had the highest theoretical density when SPSed of the mechanically alloyed powders. A correlation between crystallite size and final SPS density can be noted from Figure 4.18. The evolutions of microstructure of HfB_2 of the as-received to SPSed and annealed for 24 h at 800 ^oC were obtained by plotting $\beta_t\cos\theta$ vs. $\sin\theta$ in Figure 4.19 for each XRD reflections. Qualitative changes in crystallite size can been observed as the change in the intercept of linear fit of the data points. Qualitative changes in lattice strain were observed by noting the difference in the slopes of the linear fit lines. From the Williamson-Hall plots, annealing and SPS were seen to decrease the crystallite size and increase strain. The increase in strain is likely due to the migration of tramp solutes throughout the crystal lattice [11].

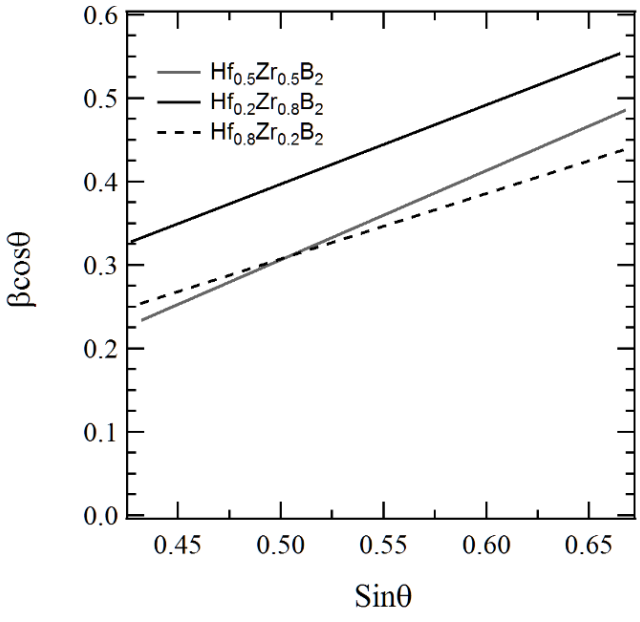

Figure 4.18 Williamson-Hall plots for milled $Hf_{0.5}Zr_{0.5}B_2$, $Hf_{0.2}Zr_{0.8}B_2$, and $Hf_{0.8}Zr_{0.2}B_2$.

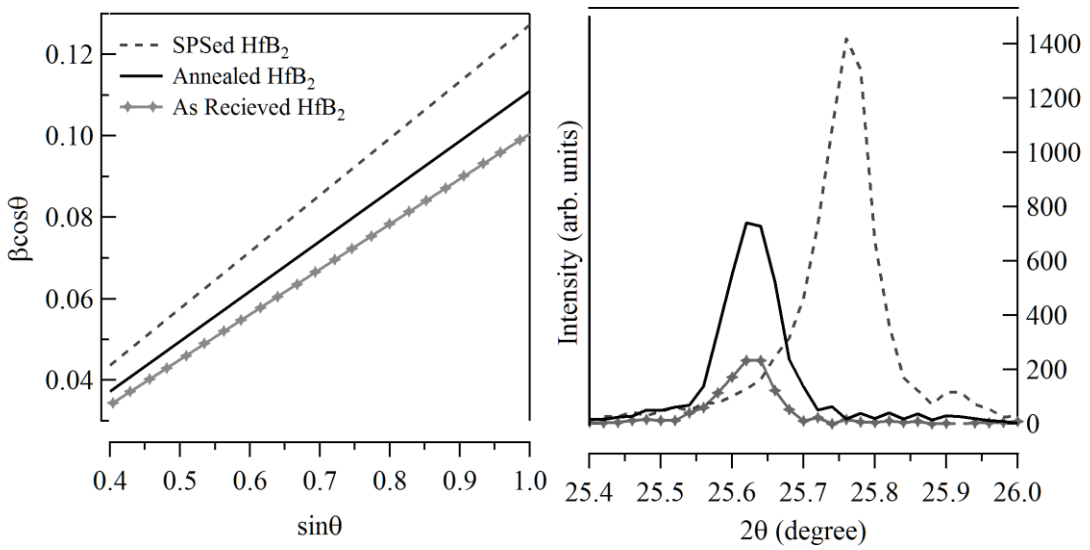

Figure 4.19. Williamson-Hall plot for the evolution of HfB_2 from as-received to SPS. Annealing of HfB_2 at 800 ^oC for 24 h under ultra-high purity argon introduced strain and decreased crystallite size.

The Qualitative evolution of strain and crystallite size for ZrB_2 is shown in Figure 4.20. Annealing ZrB_2 for 24 h at 800 ^oC in ultra-high purity argon led to a change in the lattice parameter. A slight increase in strain is observed in SPSed ZrB_2 compared to as-received powder. Crystallite size was seen to increase in annealed powder, as well as, a sharp increase in strain. The sharp increase of strain was likely due to tramp impurities in the as-received powder diffusing into the crystallites [11].

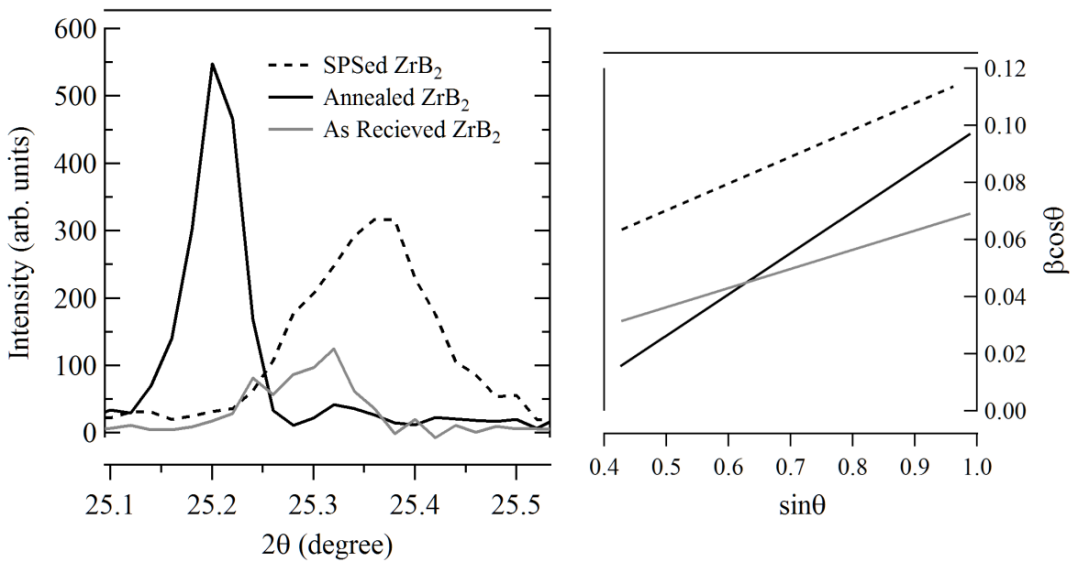

Figure 4.20. Williamson-Hall plot for the evolution of ZrB_2 from as-received to SPS. Annealing of ZrB_2 at 800 ^oC for 24 h under ultra-high purity argon introduced strain and increased crystallite size.

Existence of solid solution formation of HfB_2-ZrB_2 via SPS was confirmed by the presence of XRD patterns for P6/mmm AlB_2 type hexagonal diboride phase, and lattice constants exhibiting a linear relationship as compared to the mole fraction of its constituents. Annealing of HfB_2 and ZrB_2 as- received powders were noted to increase strain. Although the SPS dwell time for HfB_2 was 30% that of the other SPSed materials, HfB_2 exhibited higher density than ZrB_2 or $Hf_xZr_{(1-x)}B_2$ solid solutions. Electrical resistivity measurements at room temperature indicate that $Hf_{0.5}Zr_{0.5}B_2$ has a lower resistivity than that of HfB_2 or ZrB_2 individually, while $Hf_{0.2}Zr_{0.8}B_2$ and $Hf_{0.8}Zr_{0.2}B_2$ have a similar electrical resistivity as their largest constituent component. Compared to results of previous studies found in the literature, ZrB_2 and HfB_2 in the present study are characterized as having electrical resistivity slightly less than those of previous studies [10]. Vickers hardness of 20.07 GPa was obtained for the SPSed HfB_2 as compared to 12.86 GPa in SPSed ZrB_2. The deviations of the hardness in

monolithic ZrB_2 and ZrB_2 bearing composites, from literature, are likely due to impurities in the commercial ZrB_2 [10].

4.3 Characterization of SPSed $Hf_{0.5}Zr_{0.5}B_2$ Solid Solutions Containing Gd_2O_3, LaB_6, Ta, Zr, or Hf.

Because $Hf_{0.5}Zr_{0.5}B_2$ was shown to have the lowest room temperature electrical resistivity of the ZrB_2-HfB_2 solid solutions, it was chosen to be the base material for study. Additives were combined with $Hf_{0.5}Zr_{0.5}B_2$ in order to determine the effect of the additives on the microstructure and the room temperature electrical resistivity. Additives were added to $Hf_{0.5}Zr_{0.5}B_2$ because the base material showed the lowest overall room temperature electrical resistivity from the materials of Section 4.2. Additives were chosen to maintain the P6/mmm hexagonal crystal structure and others increase oxidation resistance [10]. Another purpose of this study was to address the low densification found after SPS of $Hf_{0.5}Zr_{0.5}B_2$. In Section 4.2, the base material did not achieve full densification, rather only 76.2% TD. Mechanical alloying was performed in a manner equivalent to that of Section 4.2, and SPS parameters are listed in Table 3.1. A FEG-SEM micrograph of milled $Hf_{0.5}Zr_{0.5}B_2$ + Ta (B/Me = 1.86) is shown in Figure 4.21. To the base material, Gd_2O_3 was added to increase oxidation resistance. In other samples, Ta, Hf, Zr and LaB_6 were added to the base material as sintering aids [10, 19, 60]. Elemental additives were added to the base material to bring the boron/metal molar ratios of samples to 1.86 [60].

The use of sintering aids has shown to drastically increase final density of the material as compared to $Hf_{0.5}Zr_{0.5}B_2$ alone. It is clearly evident that the agglomerates of powder after milling contained particles of nanometer scale.

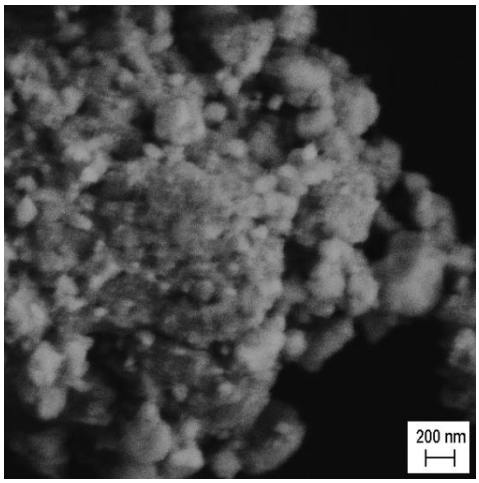

Figure 4.21 FE-SEM micrograph of milled $Hf_{0.5}Zr_{0.5}B_2$ +Ta (B/Me = 1.86).

A micro-indentation on the surface of $Hf_{0.5}Zr_{0.5}B_2$ + Zr (B/Me =1.86) is shown in Figure 4.22. The brittle nature of the materials is evident by the cracking of the material along the edges of the indentation.

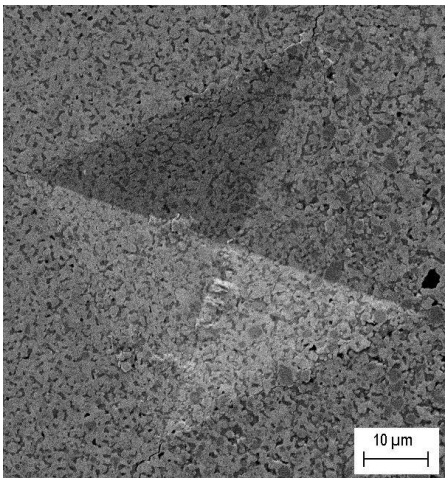

Figure 4.22 Micro-indentation hardness indentation of the polished surface of $Hf_{0.5}Zr_{0.5}B_2$ + Zr (B/Me =1.86) imaged under FEG-SEM.

During Vickers micro-indentation hardness testing, most of the materials formed cracks emanating from the corners of the micro-indentation [11]. The cracks caused by Vickers micro-indentation of $Hf_{0.5}Zr_{0.5}B_2$ +1.8 mol% Gd_2O_3 is shown in Figure 4.23.

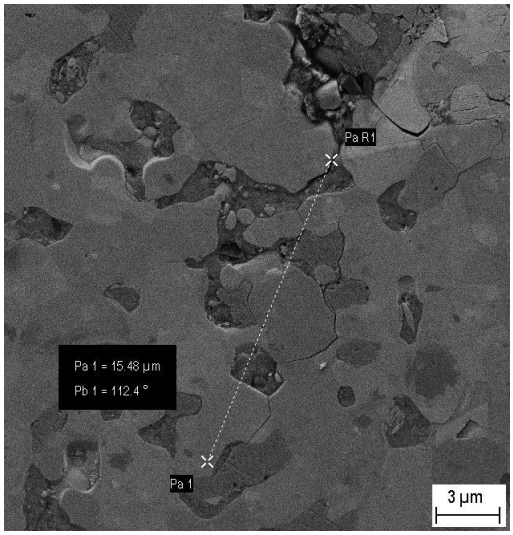

Figure 4.23 Stress crack at the corner of a micro-indentation on the surface of $Hf_{0.5}Zr_{0.5}B2$ +1.8 mol% Gd_2O_3.

The physical properties of materials in this section are shown in Table 4.5. Electrical Resistivity measurements indicate that $Hf_{0.5}Zr_{0.5}B_2$ + Zr (B/Me =1.86) had the lowest overall electrical resistivity of all the samples. $Hf_{0.5}Zr_{0.5}B_2$ +1.8 mol% LaB_6 achieved the highest final densification, and largest average grain size of all the samples.

Table 4.5 Physical properties for $Hf_{0.5}Zr_{0.5}B_2$ solid solutions containing Ta, Zr, Hf, Gd_2O_3, or LaB_6.

Sample Identifier	Density (g/cm^3)	Relative Density (%)	Hardness (GPa)	Electrical Resistivity (µΩ-cm)	Average Grain Size (µm)
$Hf_{0.5}Zr_{0.5}B_2$ +Ta (B/Me =1.86)	8.215	94.6	5.32	17.3	0.45 ± 0.46
$Hf_{0.5}Zr_{0.5}B2$ + Zr (B/Me =1.86)	7.801	94.8	5.82	8.4	1.1 ± 0.9
$Hf_{0.5}Zr_{0.5}B_2$ + Hf (B/Me =1.86)	8.250	96.2	12.04	11.6	0.54 ± 0.48
$Hf_{0.5}Zr_{0.5}B_2$ +1.8 mol% LaB_6	7.957	97.2	3.72	12.2	4.4 ± 2.6
$Hf_{0.5}Zr_{0.5}B_2$ +1.8 mol% Gd_2O_3	7.418	89.5	5.92	12.4	2.1 ± 1.2

The grain size distribution of each sample was generated from measurements made from BSE-SEM micrographs. Grain size distributions are shown in Figure 4.24. Grain size distrubutions were calculated from grain size measurements using Image J [113]. The largest distribution of grain sizes was seen with $Hf_{0.5}Zr_{0.5}B_2$ + 1.8 mol% LaB_6. Samples with elemental additives tended to have small grain sizes, some of which were in the hundreds of nanometer range. $Hf_{0.5}Zr_{0.5}B_2$ + 1.8 mol% Gd_2O_3 was seen to have a bimodal grain size distribution, 1.5 and 2.8 µm, respectively. The grain size distribution of $Hf_{0.5}Zr_{0.5}B_2$ + Hf (B/Me = 1.86) is unimodal, with the most observed grain diameter being less than 0.5 µm. $Hf_{0.5}Zr_{0.5}B_2$ + 1.8 mol% LaB_6 had a bimodal grain size distribution with the largest occurring grain size as 3 and 4 µm, respectively. The grain size distribution of $Hf_{0.5}Zr_{0.5}B_2$ + Ta (B/Me = 1.86) was found to be unimodal with the most grain diameters less than 0.5 µm. $Hf_{0.5}Zr_{0.5}B_2$ + Zr (B/Me = 1.86) grain size was unimodal with the largest occurrence of grain sizes at about 0.75 µm.

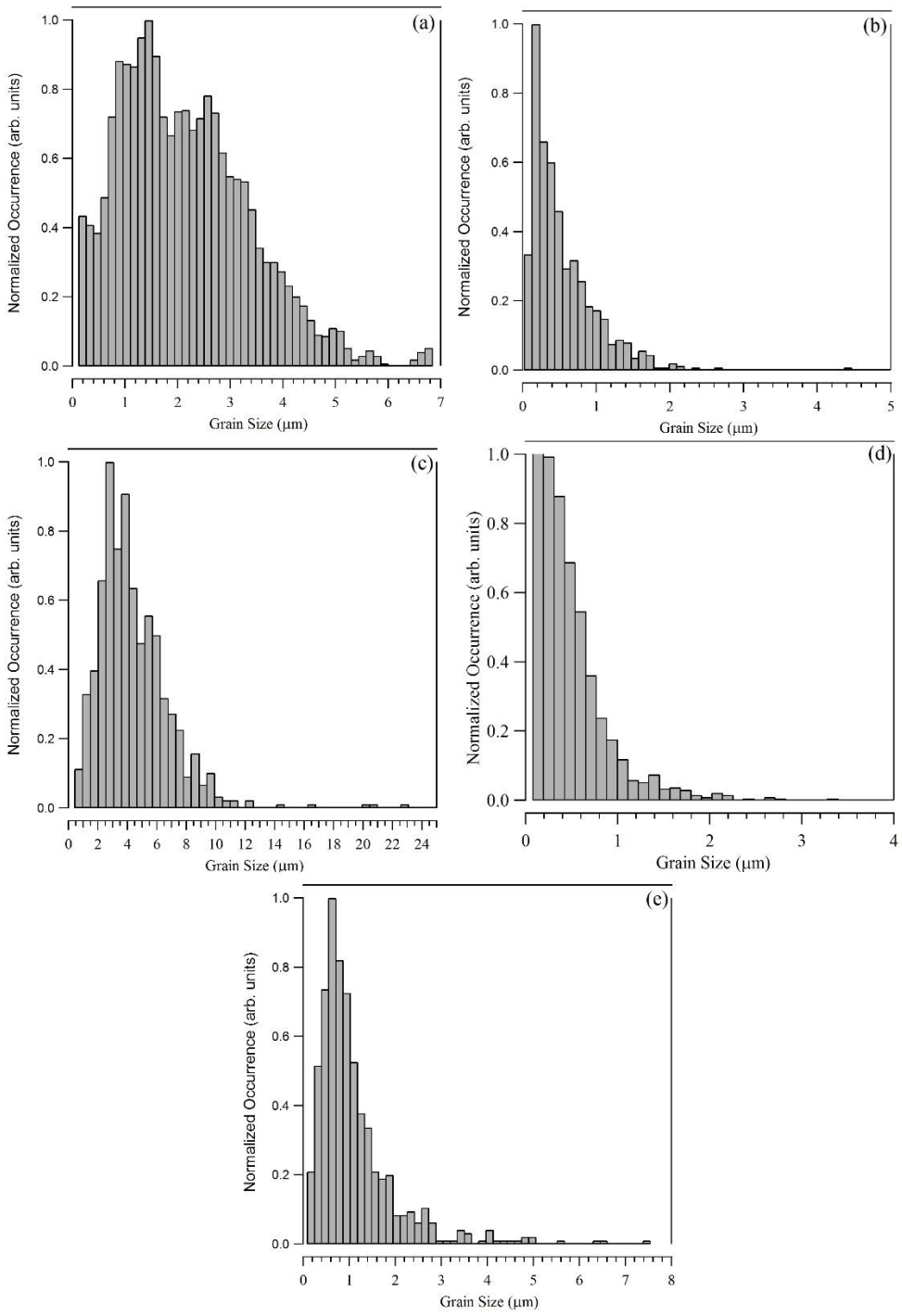

Figure 4.24 Grain size distributions of $Hf_{0.5}Zr_{0.5}B_2$ + 1.8 mol% Gd_2O_3 (a), $Hf_{0.5}Zr_{0.5}B_2$ + Hf (B/Me = 1.86) (b), $Hf_{0.5}Zr_{0.5}B_2$ + 1.8 mol% LaB_6 (c), $Hf_{0.5}Zr_{0.5}B_2$ + Ta (B/Me = 1.86) (d), $Hf_{0.5}Zr_{0.5}B_2$ + Zr (B/Me = 1.86) (e), calculated from Image J analysis.

Stripes of dense regions with small grains can be observed in the BSE-SEM micrographs as shown in Figure 4.25. The stripes of dense regions is likely due to temperature gradients created within the SPS tooling, leading to density gradients in the SPSed materials [112]. Much of the dark regions appearing in Figure 4.25 are planar porosity. Figure 4.25 (b,d,e) are BSE-SEM micrographs of $Hf_{0.5}Zr_{0.5}B_2$ containing Hf, Ta, Zr, respectively.

Materials with elemental additives are found to contain nano-sized grains within the areas of higher density. The addition of elemental additives to $Hf_{0.5}Zr_{0.5}B_2$ caused limited grain growth during SPS. Grain growth was seen during SPS of the specimen containing LaB_6. The $Hf_{0.5}Zr_{0.5}B_2$ +1.8mol% LaB_6 specimen is the only sample tested in this study that had a final grain size, after SPS, that was larger than $Hf_{0.5}Zr_{0.5}B_2$ individually.

All other specimens SPSed in this section had final grain sizes smaller than that of $Hf_{0.5}Zr_{0.5}B_2$ individually. The lack of grain growth in the samples is likely due to the promotion of densification mechanisms and the subsequent suppression of grain growth mechanism during SPS. All samples had final densities after SPS, higher than that of $Hf_{0.5}Zr_{0.5}B_2$ individually, even-though SPS parameters were quite similar. The $Hf_{0.5}Zr_{0.5}B_2$ +1.8mol% Gd_2O_3 specimen had slightly less grain growth than SPSed $Hf_{0.5}Zr_{0.5}B_2$, likely due to the formation of heterogeneous oxide scale with that of the oxide coating on the boride based powder particles during SPS. The heterogeneous oxide scale likely diminished evaporation-condensation mechanisms of the boric acid scale, and possibly affected surface diffusion rates during SPS.

The lattice parameters for the XRD reflections corresponding to the indexed P6/mmm hexagonal structure were calculated and are shown in Table 4.6.

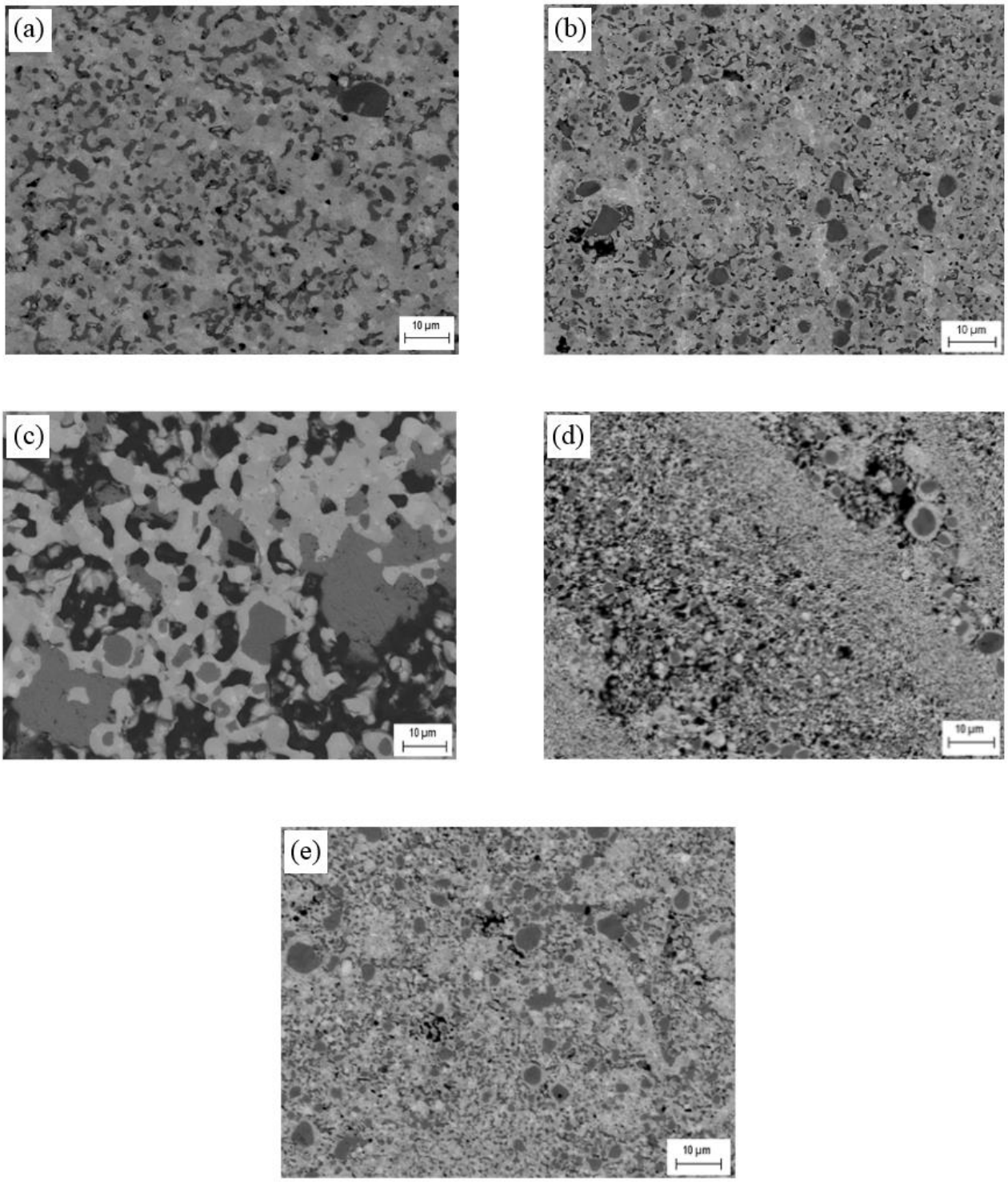

Figure 4.25 BSE micrographs of: $Hf_{0.5}Zr_{0.5}B_2$ + 1.8 mol% Gd_2O_3 (a), $Hf_{0.5}Zr_{0.5}B_2$ + Hf (B/Me = 1.86) (b), $Hf_{0.5}Zr_{0.5}B_2$ + 1.8 mol% LaB_6 (c), $Hf_{0.5}Zr_{0.5}B_2$ + Ta (B/Me = 1.86) (d), $Hf_{0.5}Zr_{0.5}B_2$ + Zr (B/Me = 1.86) (e).

Table 4.6. Lattice parameters for $Hf_{0.5}Zr_{0.5}B_2$ solid solutions containing Ta, Zr, Hf, Gd_2O_3, or LaB_6.

Sample Identifier	Lattice Parameter, a (*Å*)	Lattice Parameter, c (*Å*)
$Hf_{0.5}Zr_{0.5}B_2$ + Ta	3.144	3.466
$Hf_{0.5}Zr_{0.5}B2$ + Zr	3.145	3.486
$Hf_{0.5}Zr_{0.5}B_2$ + Hf	3.146	3.487
$Hf_{0.5}Zr_{0.5}B_2$ + LaB_6	3.147	3.490
$Hf_{0.5}Zr_{0.5}B_2$ + Gd_2O_3	3.149	3.484

SPSed $Hf_{0.5}Zr_{0.5}B_2$ solid solutions containing Ta, Zr, Hf show presence of monoclinic HfB_2 and ZrB_2 in the XRD patterns [38]. Although care was taken to eliminate contamination of milled powder from atmospheric oxygen during milling, it is likely that oxides present on the as- received Ta, Zr, Hf powders contributed to the contamination of oxides seen in the XRD patterns of SPSed materials. Figure 4.26 shows the XRD patterns observed from SPSed $Hf_{0.5}Zr_{0.5}B_2$ solid solutions containing Ta, Zr, Hf, Gd_2O_3, or LaB_6. It is apparent, from the XRD pattern of $Hf_{0.5}Zr_{0.5}B_2$ solid solutions containing Gd_2O_3 did not form a solid solution, but rather formed an oxide dispersed composite material [52]. $Hf_{0.5}Zr_{0.5}B_2$ solid solutions containing LaB_6 showed the least contamination of all the materials tested.

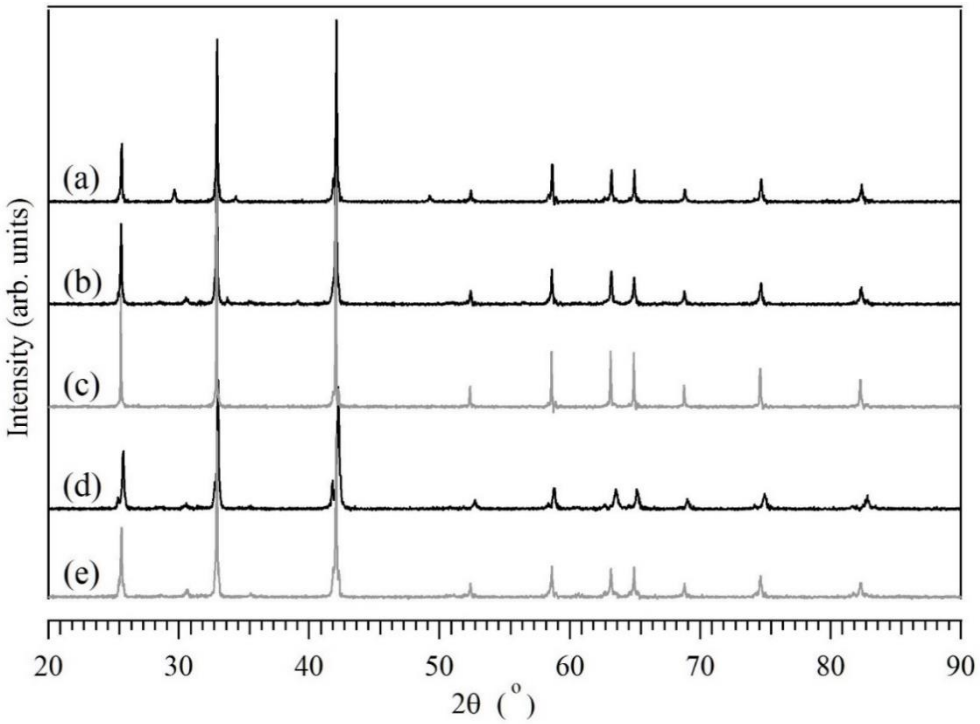

Figure 4.26 Offset XRD patterns for SPSed samples: $Hf_{0.5}Zr_{0.5}B_2$ + 1.8 mol% Gd_2O_3 (a), $Hf_{0.5}Zr_{0.5}B_2$ + Hf (B/Me = 1.86) (b), $Hf_{0.5}Zr_{0.5}B_2$ + 1.8 mol% LaB_6 (c), $Hf_{0.5}Zr_{0.5}B_2$ + Ta (B/Me = 1.86) (d), $Hf_{0.5}Zr_{0.5}B_2$ + Zr (B/Me = 1.86) (e).

5. Conclusions

From preliminary studies, it was shown that mechanochemical synthesis of ZrB_2 yielded an effectively equivalent material as that of commercially available ZrB_2. A solid solution of ZrB_2 and HfB_2 can be obtained through high-energy ball milling of commercially available diboride starting powders.

An oxide layer on the surface of 1:1 HfB_2-ZrB_2 +20 vol% SiC +1.8mol% LaB_6 can be induced through anodization in 0.1M NH4F at 40 v for 1 h. The induced oxide layer does little to affect the oxidation rate of 1:1 HfB_2-ZrB_2 +20 vol% SiC +1.8mol% LaB_6 when exposed to super-heated air for long durations.

Additives had a profound effect on the microstructure of ZrB_2 - HfB_2 solid solutions. Additives of elemental Zr, Hf, and Ta decreased the grain size achieved. Gd_2O_3 and LaB_6 had an effect the crystal structure of ZrB_2 - HfB_2 solid solutions. Gd_2O_3 and LaB_6 had larger grain sizes, but did not form solid solutions, as expected because of the different crystallographic structures of the additives and the base material.

Additives had a great effect on the densification and sinterability of ZrB_2 -HfB_2 solid solutions, without detrimentally effecting the crystal structure. The addition of elemental Hf, Zr, and Ta allowed the retention of the p6/mmm hexagonal crystal structure of the base material. When added to the base material ($Hf_{0.5}Zr_{0.5}B_2$), the elements Hf, Zr, and Ta allowed a TD of 96.2, 94.8, and 94.6 % to be obtained. The $Hf_{0.5}Zr_{0.5}B_2$ base material, when SPSed under the same conditions without additives only achieved 76.2% TD. The addition of 1.8 mol% LaB_6 to $Hf_{0.5}Zr_{0.5}B_2$ achieved 97.2%TD under similar SPS conditions, and the addition of 1.8 mol% Gd_2O_3 had 89.5%TD. LaB_6 was found to have the greatest effect of densification of the base material, however, it did not form a solid solution. Gd_2O_3 phases are clearly evident

as reflections in the XRD pattern Although, Gd_2O_3 did not form a solid solution with the base material, the p6/mmm hexagonal structure of the base material clearly evident in the XRD pattern. Gd_2O_3 is thought to be distributed along the grain boundaries of the base material, however further studies are needed to confirm.

The ZrB_2 – HfB_2 solid solution with the lowest room temperature electrical resistivity was $Hf_{0.5}Zr_{0.5}B_2$, 5.4 μΩ-cm, respectively. All other ZrB_2 – HfB_2 solid solution were close to that of the room temperature electrical resistivity of their largest constituent component. To the $Hf_{0.5}Zr_{0.5}B_2$ solid solution base material, additives and sintering aids were seen to increase the room temperature electrical resistivity. $Hf_{0.5}Zr_{0.5}B_2$ + Zr showed the lowest electrical resistivity of the samples with additives, 8.4 μΩ-cm, respectively.

$Hf_{0.5}Zr_{0.5}B_2$ + Hf (B/Me =1.86), $Hf_{0.5}Zr_{0.5}B_2$ +1.8 mol% LaB_6 , and $Hf_{0.5}Zr_{0.5}B_2$ +1.8 mol% Gd_2O_3 show promise as good starting candidates for MHD direct power electrode materials. The relatively high theoretical densities, low electrical resistivity, good hardness make these materials candidates for future studies.

6. Future Work

To complete the research of the viability of the material, described in this thesis, for use as a MHD direct power extraction electrode, further testing is required. The oxidation rate of the materials need to be determined for exposures to the oxidative conditions of MHD direct power extraction.

The hot corrosion resistance of the materials should be determined for various salts that may be used during MHD direct power extraction. A sample procedure could be as follows: to mimic the formation of a plasma during salt aspiration of the MHD direct power extraction system. A potassium salt will be electro-sprayed, at roughly 5 kV potential, onto the electrode materials to develop a thin layer of charged species from the salt, many of which may have short lifetimes. Upon deposition for a given time, the electrode material is to be heated directly with a plasma welder, until surface temperature of the sample is approximately 2400 ^{o}C. The plasma welder can be pulsed so that temperature remains at roughly 2400 ^{o}C for up to 1 h. The ideal experimental procedure would be an electrospray deposition set-up inside of a high temperature graphite furnace. The sample could be continually deposited with charged species, including ones with short lifetimes, during the temperature cycle leading to a closer representation of the actual MHD direct power extraction conditions. Appropriate gas compositions should be used in the furnace during the experiment (CO, CO_2). Discrepancies in the experiment are that short lived hydrocarbon radical species, formed during incomplete combustion, may play a role in hot corrosion rates during actual MHD direct power extraction.

Further anodization induced oxide film, oxidation resistance experiments need to be devised. The anodization induced oxide film can be grown utilizing different anodization solutions, such as dilute mixtures of strong bases or solutions of weak acids. The use of

different voltages; anodization times; and mean separations will allow fine tuning of the desired oxide morphology and thickness. It is believed that anodization induce oxide films could enhance oxidation resistance properties of the materials described in this thesis; however, the effect on the electrical properties is not currently known.

Electrochemical deposition of oxide films onto the surface of the electrode materials is also a promising method of increasing the oxidation resistance of the material; however, the effect to the materials electrical properties is not currently known.

High temperature electrical resistivity studies need to be conducted. An experiment could be as follows: a four point probe, shown in Figure 6.1, is to be connected to the sample and the sample placed in an inert atmosphere tube furnace.

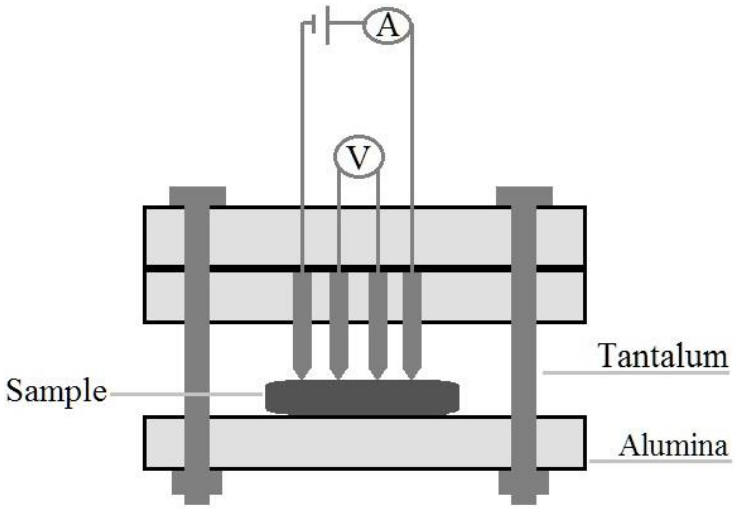

Figure 6.1 Cross sectional view of the ultra-high temperature four point probe holder.

Tantalum wires and probes could be utilized as they have melting points of about 3000 ^{o}C, as could any stable, high melting point, and conductive material. The tantalum wires should be spot welded on the ends of the tantalum probes. The ends of the probe should be machined to points within the tolerances of the test. The four point probe holder consists of

three alumina plates, four tantalum probes with tantalum wire leads, six tantalum bolts, and six tantalum nuts. Although, different combinations of plates, plate materials, and geometries of plates may be used to satisfying results. It is imperative that the bolts and nuts are torqued within tolerances (± 10 μN m) of each other to avoid unwanted dimensional changes of the plates during the experiment. Obviously, the torque on the bolts should not exceed the mechanical strength of the plates. Figure 6.2 shows a bottom view of the experimental set-up.

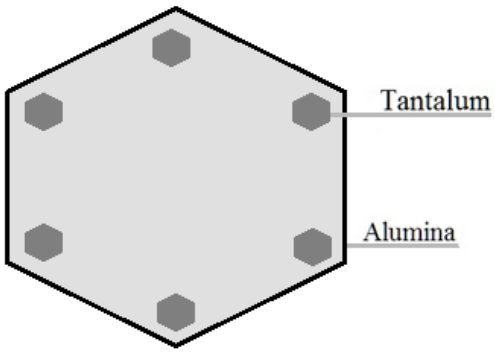

Figure 6.2 Bottom view of the ultra-high temperature four point probe assembly with the approximate bolt placements labeled as tantalum.

The probe, wire, and fastener materials shown in Figure 6.1 are represented as tantalum, although, any stable, conductive material with a high melting point could be substituted for one or all of them. The material for the wire and the probe should be kept as an identical nominal composition to minimize the thermoelectric effect. One of the alumina plates has holes drilled through its thickness to accommodate the tantalum probes. Another alumina plate has smaller holes through its thickness to allow the tantalum wires to pass through the plate. All three alumina plates have four larger holes to accommodate tantalum bolts which sandwich the sample (dark grey) between the holder and the tantalum probes in Figure 6.1.

After leaving the four point probe, the wires should be shielded utilizing alumina sheathing or beads. The furnace should provide a means for the tantalum wires to exit the furnace preferably through a vacuum grade epoxy that is able to withstand the temperature at that given point on the furnace. The two outer probes are powered by a constant current supply, and an ammeter is used to measure current that passes through the material. The two inner probes are connected to a voltmeter.

To calibrate the four point probe set-up, a nominally pure single crystal of material of known electrical resistivity, throughout the range of study, should be employed as a standard. Furnace ramp rates should be kept low in order to avoid rapid dimensional changes that may misalign the 4 point probe.

It may be desirable during future experiments to increase the grain size of $Hf_{0.5}Zr_{0.5}B_2$, containing additives, in efforts to decrease electrical resistivity and increase oxidation resistance. It is well known that electrical resistivity decreases with increasing grain size and oxidative processes tend to occur at the grain boundaries. Thus, larger grained materials tend to have high oxidation resistance, as there are less grain boundaries within the material. For ZrB_2 and HfB_2 based materials, temperatures close to 1500 ^oC have been shown to activate surface diffusion mechanisms. Surface diffusion mechanisms promote grain growth without densification. An example procedure for grain growth of the materials would include the use of a tube furnace with a continually replenished inert atmosphere. The ramp rate of the furnace should be as high as reasonable. Caution should be observed when choosing the ramp rate as many materials undergo polymorphic transformations. The ramp rate may depend on the material of the sintering boat and the tube furnace. The samples should remain in the inert

atmosphere tube furnaces, at elevated temperatures, for up to 24 h to achieve a course grained material.

The oxidation resistance, high temperature electrical resistivity, thermal conductivity, and hot corrosion resistance of the boride based materials presented in this thesis need to be addressed. The experiments outlined in this chapter will aid in the holistic understanding of the feasibility of the materials, in this thesis, to be utilized as MHD direct power electrodes.

References

1. Harada N, Kien LC, Tashiro T. Closed cycle MHD generator using He/Xe working plasma. Proceedings of the 33rd Plasmadynamics and Lasers Conference: 2002 May 20-23; Maui, HI.

2. Sherman A, Sutton GW. Engineering magnetohydrodynamics. Mineola, NY: Dover; 2006.

3. Krishnan AR, Jinshah BS. Magnetohydrodynamic power generation. Intern Jour of Sci and Res Pub 2013;3(6).

4. Karlovitz B, Halasz D. Process for the conversion of energy and apparatus for carrying out the process. US patent 2,210,918. 1940.

5. Malghan VR, History of MHD power plant development. Energy Conversion and Management, 1996;37(5):569-590.

6. Doss ED, Picologlou BF, Pan Y, Petrie T. "U-25B Magnetohydrodynamic Generator: Comparison of Analysis with Experiment", J Ener 1982;6(4):252-260.

7. Kayukawa N. Open-cycle magnetohydrodynamic electrical power generation: a review and future perspectives. Pro in Ener and Comb Sci 2004;30(1):33-60.

8. Mohan NR, Thiagarajan K, Sivan V. Studies on La(Sr)CrO_3 for use in a MHD generator. Ceram Intern 1994;20:143-146.

9. Wuchina E, Opila E, Opeka M, Fahrenholtz W, Talmy I. UHTCs: ultra-high temperature ceramic materials for extreme environment applications. The Electrochemical Society Interface 2007;16(4):30-36.

10. Fahrenholtz WG, Wuchina EJ, Lee WE, Zhou Y. Ultra-high temperature ceramics. Am Cer Soc. Hoboken, NJ: Wiley; 2014.

11. Barsoum MW. Fundamentals of ceramics. New York: McGraw-Hill; 1997.

12. Vajeeston P, Ravindran P, Ravi C, Asokamani R. Electronic structure, bonding, and ground-state properties of A1B2-type transition-metal diborides. Phy Rev B 2001;63:045115.

13. Lawson JW Jr, Bauschlicher CW, Daw MS. Ab initio computations of electronic, mechanical, and thermal properties of ZrB_2 and HfB_2. J Am Ceram Soc 2011;94 (10):3494-3499.

14. Shein IR, Ivanovski AL. Elastic properties of mono-and polycrystalline hexagonal AlB_2 like diborides of s, p and d metals from first-principles calculations. J Phys Condens Matter 2008;20:415-418.

15. Dusan LZ, Pejakovic A, Marschall J, Gasch M. Thermal and electrical transport properties of spark plasma sintered HfB_2 and ZrB_2 ceramics. J Am Ceram Soc 2011;94(80):2562-2570.

16. Mallik M, Kailath AJ, Ray KK, Mitra R. Electrical and thermophysical properties of ZrB_2 and HfB_2 based composites. J Europ Ceram Soc 2012;32:2545-2555.

17. Gasch M, Johnson S, Marschall J. Thermal conductivity characterization of hafnium diboride-based ultra-high temperature ceramics. J Am Ceram Soc 2008;91:1423-32.

18. Tye RP, Clougherty EV. The thermal and electrical conductivities of some electrically conducting compounds. Proceedings of the Fifth Symposium on Thermophysical Properties. Newton: Massachusetts; 1970 p 396-401.

19. Clougherty EV, Kalish D, Peters ET. Technical Report AMFL-TR-68-190. U.S. Air Force Materials Laboratory, Dayton, OH, 1968.

20. Samsonov GV, Kovenskaya BA, Serebryakova TI. Physical characteristics of the diborides of transition metals of groups IV and V. Soviet Phys J 1971;14 (1):11-14.3.

21. Monteverde F, Guicciardi S, Bellosi A. Advances in microstructure and mechanical properties of zirconium diboride based ceramics. Mater Sci Eng A 2003;346:310-319.

22. Melendez-Martinez JJ, Dominguez-Rodriguez A, Monteverde F, Melandri C, Portu GD. Characterization and high temperature mechanical properties of zirconium boride-based materials. J Eur Ceram Soc 2002;22:2543-2549.

23. Monteverde F. Beneficial effects of an ulta-fine αSiC incorporation on the sinterability and mechanical properties of ZrB_2. Appl Phy A 2006;82:329-337.

24. Zhu S. Densification, microstructure, and mechanical properties of zirconium diboride based ultra-high temperature ceramics [PhD thesis]. Rolla (MO): Missouri University of Science and Technology; 2008.

25. Guo S, Nishimura T, Kagawa Y. Preparation of zirconium diboride ceramics by reactive spark plasma sintering of zirconium hydride-boron powders. Scripta Mater 2011;65:1018-1021.

26. Fahrenholtz WG, Hilmas GE, Zhang SC, Zhu S. Pressureless sintering of zirconium diboride; particle size and additive effects. J Am Ceram Soc 2008;91(5):1398-1404

27. Talmy IG, Zaykoski JA, Opeka MM, Smith AH. Properties of ceramics in the zyztem ZrB2-Ta5Si3. J Mater Res 2006;21(10):2593-2599.

28. Zhang X, Xu L, Han W, Weng L, Han J, Du S. Microstructure and properties of silicone carbide whiskers reinforced zirconium diboride untra-high temperature ceramics. Solid State Sci 2009;11(1):156-161.

29. Grigoriev ON, Galanov BA, Kotenko VA, Ivanov SM, Koroteev AV, Brodnikovsky NP. Mechanical properties of ZrB2-SiC(ZrSi2) ceramics. J Eur Ceram Soc 2010;30:2173-2181.

30. Guicciardi S, Silvestroni L, Nygren M, Sciti D. Microstructure toughening mechanisms in spark plasma-sintered ZrB_2 ceramics, reinforced by SiC whiskers or SiC-chopped fiber. J Am Ceram Soc 2010;93(8):2384-2391.

31. Silvestroni L, Sciti D, Malandri C, Guiccardi S. Toughened ZrB_2-based ceramics through SiC whisker or SiC chopped fiber additions. J Eur Ceram Soc 2010;30(11):2155-2164.

32. Sciti D, Silvestroni L. Processing, sintering and oxidation behavior of SiC fibers reinforced ZrB2 composites. J Eur Ceram Soc 2012;32:1933-1940.

33. Chamberlain AL, Fahrenholtz WG, Hilmas GE. High-strength zirconium diboride-based ceramics. J Am Ceram Soc 2004;87(6):1170-1172.

34. Chamberlain AL, Fahrenholtz WG, Hilmas GE, Ellerby DT. Characterization of zirconium diboride-molybdenum disilicide ceramics. In: Bansal NP, Singh JP, Kriven WM, Schneider H. Advances in ceramic matrix composites IX vol 153. Amer Ceram Soc. Hoboken (NJ): Wiley; 2006.

35. Schneider H, editors. Advances in ceramic matrix composites IX. Westerville (OH): Am Ceram Soc; 2003. p 299-308.

36. Chamberlain AL, Fahrenholtz WG, Hilmas GE, Ellerby DT. Characterization for zirconium diboride for thermal protection systems. Key Eng Mater 2004;264-268:493-496.

37. Zhu S, Fahrenholtz WG, Hilmas GE, Zhang SC. Pressureless sintering of zirconium diboride using boron carbide and carbon additions. J Am Ceram Soc 2007;90 (11):3660-3663.

38. Zapata-Solvas E, Jayaseelan DD, Lin PBHT, Lee WE. Mechanical Properties of ZrB_2- and HfB_2 –based ultra-high temperature ceramics fabricated by spark plasma sintering. J Aur Ceram Soc 2013;33(7):1373-1386.

39. Monteverde F, Bellosi A. Beneficial effects of AlN as sintering aid on microstructure and mechanical properties of hot-preseed ZrB_2. Avd Eng Mater 2003;5(7):508-512.

40. Monteverde F, Scatteia L. Resistance to thermal shock and to oxidation of metal diborides-SiC ceramics for aerospace applications. J Am Ceram Soc 2007;94(4):1130-1138.

41. Chamberlain AL, Fahrenholtz WG, Hilmas GE. Low-temperature densification of zirconium diboride ceramics by reactive hot pressing. J Am Ceram Soc 2006;89(12):6368-6375.

42. Patel M, Reddy JJ, Prasad VVB, Jayaram V. Strength of hot pressed ZrB_2-SiC composite after exposure to high temperatures (1000-1700^{o}C). J Eur Ceram Soc 2012;32(16):4455-4467.

43. Zhu S, Fahrenholtz WG, Hfilmas GE. Influence of silicon carbide particle size on the micro-structure and mechanical properties of zirconium diboride-silicon carbide ceramics. J Eur Ceram Soc 2007;27:2077-2083.

44. Silvestroni L, Sciti D, Bellosi A. Microstructure and properties of pressureless sintered HfB2-based composites with additions of ZrB_2 or HfC. Adv Eng Mater 2007;9:915–920.

45. Telle R., Sigl LS, Takagi K. Boride-based hard materials. In Riedel R, editor. Handbook of ceramic hard materials, Vol 1. Chinchester: Wiley-VCH; 2000. p 802-945.

46. Clougherty EV, Hill RJ, Rhodes WJ, Peters ET. Research and development of refractory-oxidation resistant diborides part II, volume II: processing and characterization. Technical Report AMFL-TR-68-190, Wright-Patterson Air Force Base (OH): Air Force Materials Laboratory; January 1970.

47. McHale AE, editor. Phase diagrams for chemists volume x: borides, carbides, and nitrides. Westerville, Am Ceram Soc; 1994. Figure 8672.

48. Rezaie A, Fahrenholtz WB, Hilmas GE. Effect of hot pressing time and temperature on the microstructure and mechanical properties of ZrB_2-SiC. J Mater Sci 2007;42(8):2735-2744.

49. Watts J, Hilmas GE, Fahrenholtz WG. Mechanical characterization of ZrB_2-SiC composites with varying SiC particle sizes. J Am Ceram Soc 2011;94(12):4410-4418.

50. Chamberlain AL, Fahrenholtz WG, Hilmas GE. Low-temperature densification of zirconium diboride ceramics by reactive hot pressing. J Am Ceram Soc 2006;89(12):3638-3645.

51. Opeka MM, Talmy IG, Zaykoski, JA. Oxidation-based material selection for 2000^{o}C+ hypersonic aerosurfaces: theoretical considerations and historical experience. J Mater Sci 2004;39:5887-5904.

52. Jayaseelan, DD, Zapata-Solvas E, Brown P, Lee, WE. In situ formation of oxidation resistant refractory coatings on SiC-reinforced ZrB_2 ultra high temperature ceramics. J Am Ceram Soc 2012;95:1247–1254.

53. Han WB, Hu P, Zhang XH, Han JC, Meng SH. High-temperature oxidation at 1900°C of ZrB2–SiC ultrahigh-temperature ceramic composites. J Amer Cer Soc 2008;91:3328–3334.

54. Shugart K, Opila E, Fahrenholtz B. SiC depletion in ZrB2-30 vol% SiC at ultrahigh temperatures. J Amer Cer Soc, 2015;98(5):1673-1683.

55. Zhang XH, Hu P, Han Xu L, Meng SA. The addition of lanthanum hexaboride to zirconium diboride for improved oxidation resistance. Scripta Mater 2007;57:1036-1039.

56. Eakins E, Jayaseelan DD, Lee WE. Toward oxidation-resistant ZrB_2-SiC ultra high temperature ceramics. Metal Mater Trans A, 2010;878-887.

57. Levine SR, Opila EJ. Tantalum addition to zirconium diboride for improved oxidation resistance. In: Proceedings of 27th Annual Conference on Composites, Materials and Structures: 2003 Jan 27-31; Cape Canaveral, FL; 2003. Report No. NASA/TM—2003-212483.

58. Talmy IG, Zaykoski JA, Opeka MM, Dallek S. Oxidation of ZrB_2 ceramics modified with SiC and group IV–VI transition metal borides. In: McNallan M, Opila E, editors. High

temperature corrosion and materials chemistry III. Pennington (NJ): The Electrochemical Society, Inc; 2001. p 144.

59. Opila E, Levine S, Lorincz J. Oxidation of ZrB_2 and HfB_2-based ultra-high temperature ceramics: effect of Ta additions. J Mater Sci 2004;39(19):5969-5977.

60. Kaufman L, Clougherty EV. Investigation of boride compounds for very high temperature application. Report Number RTD-TDR-63-4096, Part II. Wright-Patterson Air Force Base (OH): Air Force Materials Laboratory; February 1965.

61. Tucker SA, Moody HR. The preparation of a new metal Boride. Proc Chem Soc Lond 1901;17(238):129-130.

62. McKenna PM. Tantalum carbide: its relation to other hard refractory compounds. Ind Eng Chem 1936;28(7):767-772.

63. Agte C, Moers K. Methoden zur Reindarstellung hochschmelzender carbide, nitride, and boride und beschreibung einiger inhrer eigenschaften. Z Anog Allg Chem 1931;198(1):233-275.

64. Pierre AC. Introduction to sol-gel processing. NY: Kluwer Academic Publishers; 1998.

65. Zhang Y, Li RX, Yin S, Sato T, Li JP. Synthesis of ZrB_2–SiC composite powders by sol–gel method using acetic acid as chemical modifier. J Taiwan Inst of Chem Eng 2015;46:200-204.

66. Ang C, Seeber A, Wang K, Cheng YB. Modification of ZrB_2 powders by a sol–gel ZrC precursor—a new approach for ultra high temperature ceramic composites. J Asian Ceram Soc 2013;1(1):77-85.

67. Zhao H, He Y, Jin Z. Preparation of zirconium boride powder. J Amer Ceram Soc 1995;78(9):2534–2536.

68. Qiu HY, Guo WM, Zou J, Zhang GJ. ZrB_2 powders prepared by boro/carbothermal reduction of ZrO_2: the effects of carbon source and reaction atmosphere. Powder Tech 2012;217:462-466.

69. Jung EY, Kim JH, Jung SH, Choi SC. Synthesis of ZrB_2 powders by carbothermal and borothermal reduction. J Alloys Comp 2012;538:164-168.

70. Peshev P, Bliznakov G. On the borothermic preparation of titanium, zirconium and hafnium diborides. J Less Common Metals 1968;14(1):23-32.

71. Zheng YT, Li HB, Xu ZH, Zhao J, Yang P. Reaction mechanism of self-propagating magnesiothermic reduction of ZrB_2 powders. Rare Metals 2013;32(4):408-413.

72. Setoudeh N, Welham NJ. Formation of zirconium diboride (ZrB_2) by room temperature mechanochemical reaction between ZrO_2, B_2O_3 and Mg. J Alloys and Compounds 2006;420(1-2):225-228.

73. Sonber JK, Suri AK. Synthesis and consolidation of zirconium diboride: review. Adv App Ceram 2011;110(6):321.

74. Avile´s MA, Co´rdoba JM, Sayague´s MJ, Alcala´ MD, Gotor FJ. Mechanosynthesis of $Hf_{1-x}Zr_xB_2$ solid solution and $Hf_{1-x}Zr_xB_2$/SiC composite powders. J Am Ceram Soc 2010;93(3):696–702.

75. Suryanarayana C. Recent developments in mechanical alloying 203. Rev Adv Mater Sci 2008;18:203-211.

76. Bernotat S, Sch¨onert K. Size reduction. In: Ullmann's Encyclopedia of Industrial Chemistry. VCH Verlagsgesellschaft, Weinheim 1998;B2:5.1–5.39.

77. Abdellaoui M, Gaffet E. The physics of mechanical alloying in a modified horizontal rod mill: mathematical treatment. Acta Mater 1996;44:725–734.

78. Suryanarayana C, Ivanov E, Boldyrev VV. The science and technology of mechanical alloying. Mat Sci Eng A 2001;304–306:151–158.

79. Bernhardt C, Heegn, HP. (1976a) Contribution to the investigation of the mechanical activation in fine grinding mills. In: Rumpf H Sch¨onert K editors. Proc. IVth European Symp. On Comminution. N¨urnberg 1975, Dechema Monographien, Bd. 79, Verlag Chemie, Frankfurt am Main. p 213–225.

80. Juh´asz AZ, Opoczky L. Mechanical activation of minerals by grinding: pulverizing and morphology of particles. Chichester: Ellis Horwood; 1990.

81. Calka A, Radlinski AP. Universal high performance ball milling device and its application for mechanical alloying. Mater Sci Eng A 1991;134:1350–1353.

82. Baláž P. High-energy milling: mechanochemistry in nanoscience and minerals engineering, Berlin Heidelberg: Springer-Verlag; 2008. p 103-132.

83. Fokina EL, Budim NI, Kochnev VG, Chernik GG. Planetary ball mills of periodic and continuous action. J Mat Sci 2004;39:5217–5222.

84. Schubert H. Aufbereitung fester mineralischer Rohstoffe. VEB Deutscher Verlag f¨ur Grundstoffindustrie, Leipzig, Band I; 1989.

85. P¨upke I. Construction and operating method of an attrition mill in powder metallurgy. Powder Metallurgy Int 1971;3:94–96.

86. Castro CL, Mitchell BS. Nanoparticles from mechanical attrition. In: Barton MI editor. Synthesis, functionalization and surface treatment of nanoparticles. Stevenson Ranch; Amer Sci Pub: 2002. p 1-15.

87. Koch CC. The synthesis and structure of nanocrystalline materials produced by mechanical attrition: a review. Nanostructured Materials 1993;2:109–129.

88. Avvakumov EG. Mechanical methods of chemical processes activation. Nauka, Novosibirsk; 1986.

89. Kopp-Alves A, Bergmann CP, Berutti AF. Novel synthesis and characterization of nanostructured materials, engineering materials. Berlin Heidelberg: Springer-Verlag; 2013.

90. Borner I, Eckert J. Nanostructure formation and steady-state grain size of ball-milled iron powders. Mater Sci Eng A 1997;226-228:541-545.

91. Beenken W, Gock E, Kurrer KE. The outer mechanics of the eccentric vibration mill. Int J Min Proc 1996;44–45:437–446.

92. Suryanarayana C. Mechanical alloying and milling. Prog Mater Sci 2001;46:1-184.

93. Bal´aˇz P, Godoˇc´ıkov´a E, Kril'ov´a L, Lobotka P, Gock E. Preparation of nanocrystalline materials by high-energy milling. Materials Science Engineering A 2004;386:442–446.

94. Takacs L, McHenry JS. Temperature of the milling balls in shaker and planetary mills. J Mat Sci 2006;41:5246–5249.

95. Beke B. Considerations about the energetic effectivity of fine grinding. In: Iinoya K, Beddow JK, Gimbo G, editors. Proc Int Symp on Powder Technology. Washington: Hemisphere Pub Cor; 1984. p373–379.

96. Davis RM, Koch CC. Mechanical alloying of brittle components: silicon and germanium. Scrip Metal 1987;21:305–310.

97. Koch CC. Synthesis of nanostructured materials by mechanical milling: problems and opportunities. Nanostructured Materials 1997;9:13–22.

98. Ogino Y, Yamasaki T, Atzumi N, Yoshioka K. Nitriding of transition metal powders by ball milling in nitrogen gas. Materials Transactions JIM 1993;34:1212–1216.

99. Boldyrev VV, Tk´aˇcov´a K. Mechanochemistry of solids: past, present and prospects. J of Mat Syn 2001;8:121–132.

100. Glass SJ, Ewsuk KG. Ceramic powder compaction. MRS Bulletin 1997;22:24–28.

101. Riedel R, Chen IW. Ceramics science and technology: volume 3: synthesis and processing. First Ed. KGaA. Wiley-VCH: Verlag GmbH & Co; 2012.

102. Piccolroaz A, Bigoni D, Gajo A. An elastoplastic framework for granular materials becoming cohesive through mechanical densification. Part I - small strain formulation. Euro J Mech A: Solids 2006;25:334-357.

103. Piccolroaz A, Bigoni D, Gajo A. An elastoplastic framework for granular materials becoming cohesive through mechanical densification. Part II - the formulation of elastoplastic coupling at large strain. Euro J Mech A: Solids 2006;25:358-369.

104. Erlich, DC, Curran DR. Characterization of the dynamic behavior of porous solids, part 6: dynamic response of porous ceramics. SRI International Report DNA 3961F-6. 1976.

105. German RM. Sintering theory and practice. NY: Wiley-VCH; 1996.

106. Olevsky E, Bogachev I, Maximenko A. Spark-plasma sintering efficiency control by inter-particle contact area growth: a viewpoint. Scripta Mater 2013;69(2):112-116.

107. Munir ZA, Anselmi-Tamburini U, Ohyanagi M. The effect of electric field and pressure on the synthesis and consolidation of materials: a review of the spark plasma sintering method. J Mat Sci 2006;41(3):763-777.

108. Sonber JK, Suri AK. Synthesis and consolidation of zirconium diboride: a review. Adv App Ceram 2011;110(6),321-334.

109. Olevsky EA, Garcia-Cardona C, Bradbury WL, Haines CD, Martin DG, Kapoor D. Fundamental aspects of spark plasma sintering: II. Finite Element Analysis of Scalability. J Am Ceram Soc 2012;95:2414–2422.

110. Olevsky EA, Froyen L. Impact of thermal diffusion on densification during SPS. J Amer Ceram Soci 2009;92:S122–S132.

111. Guillon O, Gonzalez-Julian J, Dargatz B, Kessel T, Schierning G, Räthel J, Herrmann M. Field-assisted sintering technology/spark plasma sintering: mechanisms, materials, and technology developments. Adv Eng Mater 2014;16:830–849.

112. Giuntini D, Raethel J, Herrmann M, Michaelis A, Olevsky EA. Advancement of tooling for spark plasma sintering. J Am Ceram Soc 2015;98:3529–3537.

113. ImageJ. (n.d.). Retrieved November 1, 2015, from http://imagej.nih.gov/ij/